Science Robotics
AAAS

Supplementary Materials for

Remote control of muscle-driven miniature robots with battery-free wireless optoelectronics

Yongdeok Kim *et al.*

Corresponding author: Rashid Bashir, rbashir@illinois.edu; John A. Rogers, jrogers@northwestern.edu; Mattia Gazzola, mgazzola@illinois.edu

Sci. Robot. **7**, eadd1053 (2023)
DOI: 10.1126/scirobotics.add1053

The PDF file includes:

Other Supplementary Material for this manuscript includes the following:

Supplementary Methods

Characterizations of optical irradiance of wireless optogenetic devices

Optical irradiance characterization was performed in two complementary steps using an external power supply. First, the I-V characteristic of the μ-ILED (460 nm; SunLED) was obtained using a semiconductor device analyzer (Keysight 1500A) connected to an electrical probe station (Signatone 1160) (fig. S3 (a)). This characterization yields the electrical power of the μ-ILED with respect to go through current. Then, the optical output power was obtained with an integrating sphere (FOIS-1, Ocean Optics), calibrated by a standard diffusive light source (HL-3 Plus, Ocean Optics) for different input currents, driven by the semiconductor device analyzer (fig. S3 (b) and (c)). This optical power, in conjunction with respective electrical power, yields the efficiency of the μ-ILEDs (fig. S3 (d)).

The second step involved measurements of go through current of individual μ-ILED for both passive and active optogenetic devices during operation with respect to transmission antenna power, tilt angle, and locations. The outcome results, combined with obtained I-V characteristics and efficiency, yield the electrical power and the respective optical irradiance of the individual μ-ILED during operation. Results are included in fig. S3-S5.

Myotube alignments and surface radiosity analysis

To predict the locomotion of eBiobot corresponds to the different configurations of 5 μ-ILEDs, the superposition of myotube alignment and μ-ILED radiosity to myotubes were analyzed. ImageJ software (Orientation-J plugin) was used for the polar histogram (fig. S15), Fast Fourier Transform (FFT) analysis (fig. S16), and the determination of the vector field of the alignment of myotubes (fig. S17) from confocal microscope image in fig. S14 (c). The vector field was detected on myotubes in 10 pixels, and the distances of x- (dX) and y-axis (dY) of myotubes in each 10 pixels were analyzed (resolution of 4.07×4.07 mm confocal image is 6552×6552 pixels). Surface-to-surface radiation module (COMSOL Multiphysics 6.0) was selected to simulate the radiosity of a single and 5 μ-ILEDs with different angles to myotubes which is integrated on the skeleton based on the light intensities in fig. S9 (a). The diffuse irradiance of each μ-ILEDs is 1900 W/m^2 for 5 μ-ILEDs and 10366 W/m^2 for single μ-ILED, and the emitted irradiation direction is faced to myotubes. The distance between μ-ILEDs and surface of muscle actuator was known as 2.2 mm (1.24 mm in fig. S7 plus about 1 mm for passive strain of beam) the displacement and dimension of each μ-ILED are referred from the design of Fig. 1(a)-iii and fig. S2. The transparent refractive index of cell media is assumed as 1.345 (*31*), and the ambient emissivity of skeleton and internal myotubes were set as "0".

Friction study

The angle of repose method was used to determine the static friction coefficient by inclining the angle of the plane until the eBiobot skeleton started sliding using the customized equipment in fig. S18 (b) and (c). The friction coefficient was calculated using: $\mu = \tan\theta$ (measured angle) in fig. S18 (c). The surface of PE film (McMaster) was functionalized with different surface chemistries. Oxygen plasma (Pico Diener) was treated for 1 minute with 100 W to make the surface hydrophilic. To tune hydrophobicity, the PE surface was treated with (3-Aminopropyl)triethoxysilane (APTES) (Sigma-Aldrich) after oxygen plasma treatment. 0.2 (v/v) % APTES in ethanol was used to treat the surface for 1 minute, followed by rinsing with PBS and

this step was repeated 3 times. Further hydrophobic functionalization, the PE film was incubated in 5 (v/v) % APTES in ethanol for 2 hours in room temperature, then was rinsed with PBS. The contact angle images were taken by the Dino-lite digital microscope after adding a drop of 2 ul distilled water on surfaces.

Modeling and Simulation of Cosserat Rods

We mathematically describe a slender rod (fig. S6 (a)) by a centerline $\bar{\mathbf{x}}(s,t) \in \mathbb{R}^3$ and rotation matrix $\mathbf{Q}(s,t) \in \{\bar{\mathbf{d}}_1, \bar{\mathbf{d}}_2, \bar{\mathbf{d}}_3\}^{-1}$, which leads to a general relation between frames for any vector $\mathbf{v}$: $\mathbf{v} = \mathbf{Q}\bar{\mathbf{v}}$, $\bar{\mathbf{v}} = \mathbf{Q}^T\mathbf{v}$, where $\bar{\mathbf{v}}$ denotes a vector in the lab frame and $\mathbf{v}$ is a vector in the local frame. Here $s \in [0, L_0]$ is the material coordinate of a rod of rest-length L_0 , L denotes the deformed filament length and t is time. If the rod is unsheared, $\bar{\mathbf{d}}_3$ points along the centerline tangent $\partial_s\bar{\mathbf{x}} = \bar{\mathbf{x}}_s$ while $\bar{\mathbf{d}}_1$ and $\bar{\mathbf{d}}_2$ span the normal-binormal plane. Shearing and extension shift $\bar{\mathbf{d}}_3$ away from $\bar{\mathbf{x}}_s$, which can be quantified with the shear vector $\boldsymbol{\sigma} = \mathbf{Q}(\bar{\mathbf{x}}_s - \bar{\mathbf{d}}_3) = \mathbf{Q}\bar{\mathbf{x}}_s - \mathbf{d}_3$ in the local frame. The curvature vector $\boldsymbol{\kappa}$ encodes $\mathbf{Q}$'s rotation rate along the material coordinate $\partial_s\mathbf{d}_j = \boldsymbol{\kappa} \times \mathbf{d}_j$, while the angular velocity $\boldsymbol{\omega}$ is defined by $\partial_t\mathbf{d}_j = \boldsymbol{\omega} \times \mathbf{d}_j$. We also define the velocity of the centerline $\bar{\mathbf{v}} = \partial_t\bar{\mathbf{x}}$ and, in the rest configuration, the bending stiffness matrix **B,** shearing stiffness matrix **S**, second area moment of inertia **I**, cross-sectional area A and mass per unit length ρ. Then, the dynamics of a soft slender body is described by:

$$\rho A \cdot \partial_t^2\bar{\mathbf{x}} = \partial_s\left(\frac{\mathbf{Q}^T\mathbf{S}\boldsymbol{\sigma}}{e}\right) + e\bar{\mathbf{f}} \tag{1}$$

$$\frac{\rho\mathbf{I}}{e} \cdot \partial_t\boldsymbol{\omega} = \partial_s\left(\frac{\mathbf{B}\boldsymbol{\kappa}}{e^3}\right) + \frac{\boldsymbol{\kappa}\times\mathbf{B}\boldsymbol{\kappa}}{e^3} + \left(\mathbf{Q}\frac{\bar{\mathbf{x}}_s}{e} \times \mathbf{S}\boldsymbol{\sigma}\right) + \left(\rho\mathbf{I}\cdot\frac{\boldsymbol{\omega}}{e}\right)\times\boldsymbol{\omega} + \frac{\rho\mathbf{I}\boldsymbol{\omega}}{e^2}\partial_t e + e\mathbf{c} \tag{2}$$

where Eqs. (1, 2) represent linear and angular momentum balance at every cross section, $e = |\bar{\mathbf{x}}_s|$ is the local stretching factor, and $\bar{\mathbf{f}}$ and $\mathbf{c}$ are the external force and couple line densities, respectively (shown in fig. S6 (b)).

For numerical implementation, the continuous representation shown above is discretized into $(n+1)$ nodes of position x_i and n connecting cylindrical segments (fig. S6 (c)). The centerline linear displacements are determined by the internal and external forces acting at the nodes (of mass m_i), while rotations are accounted for via couples applied to the cylindrical elements. The dynamic behavior of a rod is then computed by integrating the discretized set of equations in time via a second order position Verlet scheme. Details of our numerical implementation can be found in (*22*), together with a rigorous validation against a number of benchmark problems with known analytic solutions as well as verification against experimental studies involving contact, anisotropic surface friction and highly viscous fluids.

Modeling of hydrogel scaffolds via elastic filaments

The scaffolds of our eBiobots are composed by beams of rectangular cross-section. In order to properly simulate them within our Cosserat rod framework, these structures need to be converted into rods of circular cross-section (fig. S6 (d)), while conserving the original mass and moment of inertia. Thus, the following equations are applied to convert rectangular beams into rods:

$$r = \sqrt{\frac{bh}{\pi}} \tag{3}$$

$$E_{rod} = \left(\frac{bh^3}{3\pi r^4}\right)E_{beam} \tag{4}$$

where b, h and E_{beam} are the width, thickness, and Youngs modulus of the rectangular beams, and r and E_{rod} are the equivalent radius and Young's modulus of the rod, respectively. Eq. 3 ensures

that cross-sectional area and therefore mass per unit length is retained (material density kept constant, ρ_{beam}=ρ_{beam}). Eq. 4 is then used to compute the equivalent Young's modulus for the rod such that the moment of inertia is conserved. The modeling accuracy of this approach was demonstrated in (*7, 9, 10, 23*). Here, we assign the value of the Young's modulus and density of PEGDA hydrogel to E_{beam} and ρ_{beam}, respectively. Details on the parameters are provided in table S3.

Modeling of muscle tissues

Muscles in the eBiobot are modeled as an assembly of three soft filaments. Two circular filaments are constructed around the legs and are connected by a short straight filament, replicating the topology of the experimental muscle tissues. Our virtual muscles are assumed to possess bio-mechanical properties (density, Young's modulus) similar to human skeletal muscles (table S3). To incorporate muscle activities into our model, the muscle force is computed based on a constant voluntary contractile stress (σ_m), and wrapped into the external force vector $\bar{\mathbf{f}}$ in Eq. 1. We write the total force generated by muscle's contraction as:

$$F_m = \frac{A_0}{1-\epsilon}\sigma_m = F_{out} + E_m\epsilon(\frac{A_0}{1-\epsilon}) \quad (5)$$

where F_{out} is the force that muscle tissue exerts on the scaffold ("muscle output" – which is known and experimentally characterized by leg deflections), E_m is the Young's modulus of muscle, A_0 is the muscle cross-sectional area at rest, and ϵ is its local axial strain (which is a function of time). The second term on the right-hand side of Eq. 5 takes into account the additional force necessary to deform the tissue itself. At any time, this force can be written as a product of the internal elastic stress $E_m\epsilon$ (Hooke's law) and the instantaneous cross-sectional area A. Due to the incompressibility of the muscle tissue (*32*), one can write a volume conservation relation $AL = A_0L_0$ to relate A and A_0, where L and L_0 denote the contracted and resting muscle length, respectively. Given that $\frac{L}{L_0} = 1 - \epsilon$ (strain is taken positive for contraction), we then write $A = A_0/(1-\epsilon)$, hence the form of the second term on the right-hand side of Eq. 5.

The force muscle exerting on the scaffold (F_{out}) consists of two components: a quasi-static rest tension (passive force) and a time dependent active contraction force. We approximate the functional shape of a single active contraction as a Gaussian function (e^{-t^2/C^2}), therefore write F_{out} as:

$$F_{out} = F_{pass} + F_{act}\cdot e^{-\frac{t_{peak}^2}{\sigma^2}}, t_{peak} = t - \frac{n}{f}\ (n = 1,2,\dots.) \quad (6)$$

where F_{pass} and F_{act} are the magnitudes of passive tension and peak active contraction force, t is real time, f is the muscle contraction frequency, and n is the index of muscle contractions. The values of F_{pass}, F_{act} and f are experimentally determined and provided in Fig. 2 in the main text. The value of peak width ($\sigma = 0.06$) is determined by fitting to the experimentally measured muscle contraction curves. We have demonstrated that when this muscle model is incorporated into our simulations, the resulting leg deflections match the experimental data closely (Fig. 2(D)).

Interactions between filaments

The simulation of the walker involves assembling multiple rods representing different elements. Rods constituting the walker scaffold are connected using fixed joints to resist all relative

motions. To avoid the interpenetration between rods representing the muscle tissue and the skeleton, we introduce repulsive forces $\mathbf{F}_c$ acting between filaments that are in contact. Considering two rods (rod i,j, with radii r_i and r_j respectively) that are in contact, the corresponding $\mathbf{F}_c$ is stated as

$$\mathbf{F}_c = H(\epsilon_{ij}) \cdot (-k\epsilon_{ij}) \cdot \mathbf{d}_{min}^{ij} \tag{7}$$

where $\mathbf{d}_{min}^{ij}$ is the minimum distance vector between the two rods, so that the scalar overlap displacement is written as $\epsilon_{ij} = (r_i + r_j - d_{min}^{ij})$. $\mathbf{F}_c$ is then calculated based on the linear response to the interpenetration distance modulated by the stiffness k. $H(\epsilon_{ij})$is the Heaviside function that ensures a repulsion force is produced only in case of contact ($\epsilon_{ij} \geq 0$). More information about the connections and interactions between rods can be found in (*24*). Parameter values can be found in table S3.

Friction model and Hydrodynamics

We numerically account for the eBiobots' surrounding environmental physics. Walkers are fully submerged in a physiological solution while being stimulated, so gravitational and buoyant forces are applied to their bodies. We assume that the muscle tissue is neutrally buoyant in the culture media since they have very similar densities. Contact and frictional forces are applied to the skeleton to account for ground effects. We implement a simple isotropic Coulomb friction model, so that the friction force $\mathbf{F}_f$ is written as,

$$\mathbf{F}_f = \begin{cases} -\min(|\mathbf{F}_h|, \mu_s|\mathbf{F}_n|) \cdot \frac{\mathbf{F}_h}{|\mathbf{F}_h|}, & \text{if } |\mathbf{v}_h| \leq v_\epsilon \\ -\mu_k|\mathbf{F}_n| \cdot \frac{\mathbf{v}_h}{|\mathbf{v}_h|}, & \text{if } |\mathbf{v}_h| > v_\epsilon \end{cases} \tag{8}$$

where $\mathbf{F}_h$ and $\mathbf{F}_n$ denote the overall horizontal and normal force experienced by the skeleton respectively, $\mathbf{v}_h$ is horizontal velocity of the skeleton, μ_s and μ_k are the static and kinematic friction coefficients and v_ϵ represents a (small) velocity threshold to distinguish between static and kinematic coefficients (parameters are listed in table S3). Friction coefficients are selected based on the experimental characterization presented in fig. S18. Results of the frictional force and its resulting locomotion trajectory under different stimulation protocols are shown in fig. S25.

Furthermore, the motion of the walker is resisted by a drag force due to the surrounding fluid. We approximate this effect using an external damping force that is proportional to the local velocity vector ($\mathbf{v}$) of the walker. This approximation is rigorously valid only in the case of viscosity dominated flow regimes, characterized by Reynolds numbers Re<<1. Our walkers are characterized by relatively small Reynolds numbers (Re∼1) which are nonetheless sufficiently large for inertia to play a role. In these conditions, hydrodynamic loads can be accurately estimated only through direct numerical simulations which are computationally demanding and beyond the scope of this investigation. Thus, in order to provide a first order approximation, we choose to maintain the use of the low Reynolds number model, well aware of its limitations. Nevertheless, we note that the impact of hydrodynamic loads on our eBiobots' dynamics is very modest as frictional forces dominate. Then, the hydrodynamic force per unit length $\mathbf{F}_d$ acting on the rod assembly is expressed as:

$$\mathbf{F}_d = -\gamma_d \mathbf{v}, \tag{9}$$

where γ_d= 0.22g/(mms) is an empirically determined dissipation factor. More details about the numerical implementations and validations of the environmental physics can be found in (*22, 23*).

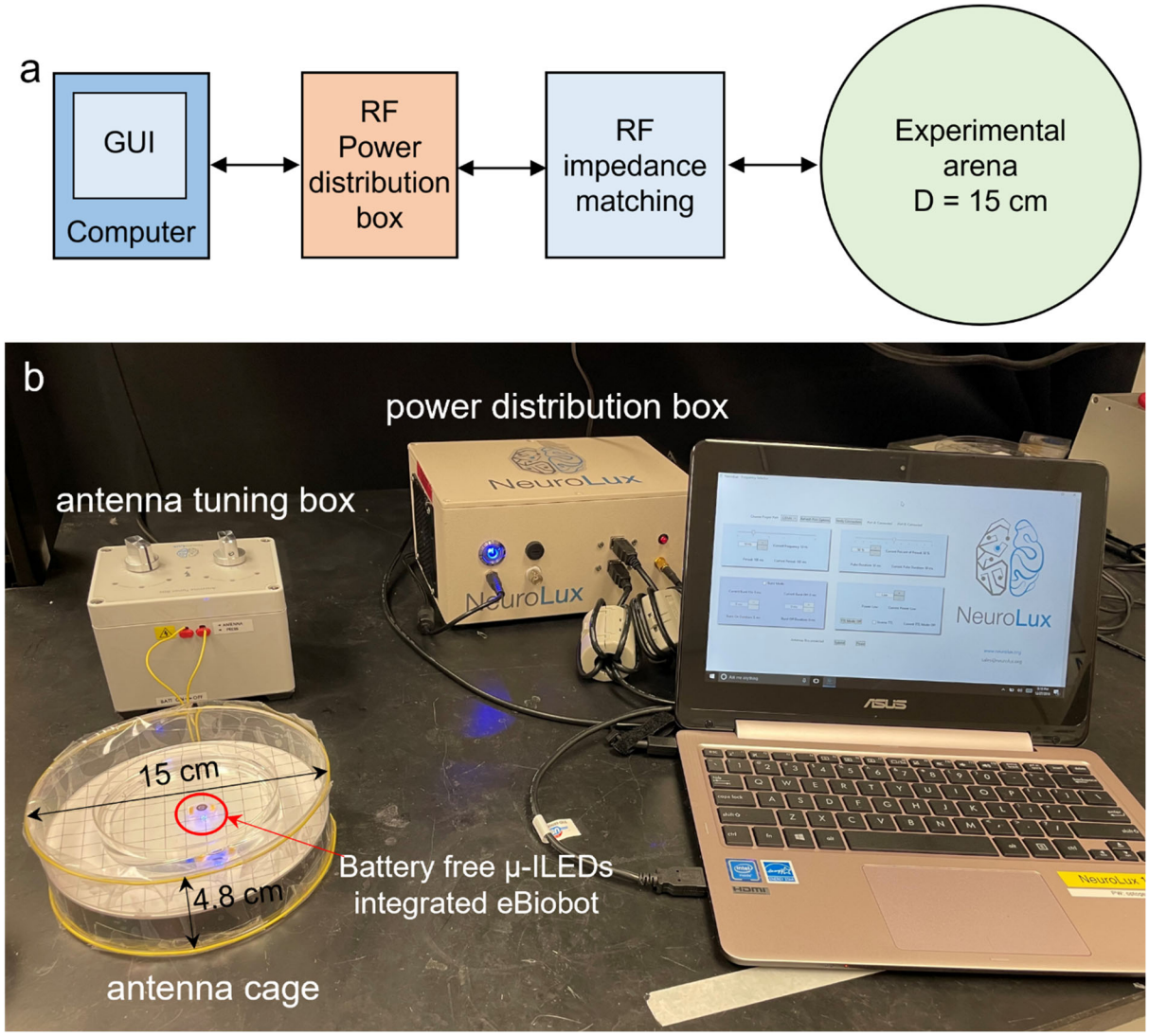

Fig. S1. Experimental set up for wireless control of eBiobot. (a) Block diagram for the wireless control of passive optogenetic devices via resonant magnetic induction. (b) Image of experimental set up for remote control of battery-free wireless passive optogenetic device integrated eBiobot using RF power distribution box, antenna impedance matching box, the laptop with the control software, and a customized antenna with a diameter of 15 cm.

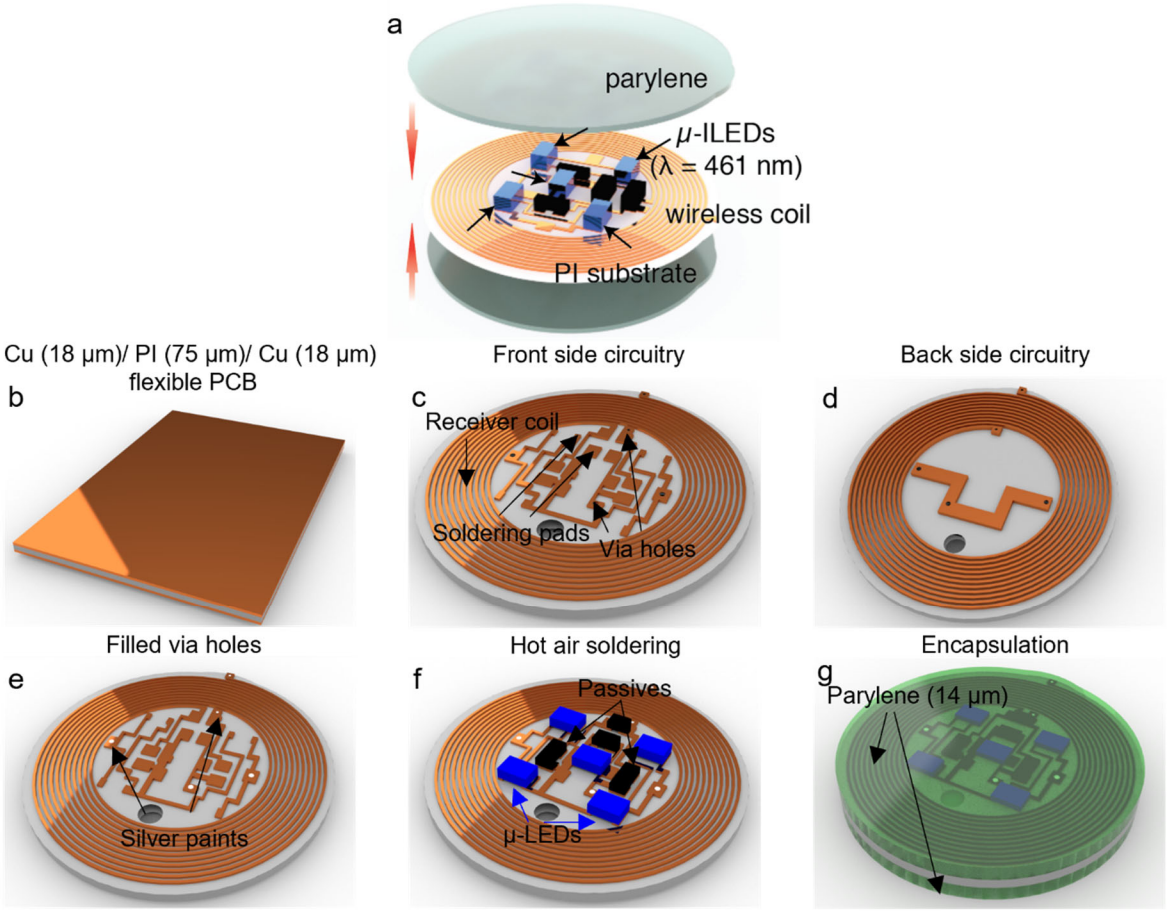

Fig. S2. Fabrication process for passive wireless optogenetic devices. (a) Layered schematics of the optogenetic device. (b) Prepare a tri-layer flexible printed circuit board (fPCB) composed of Cu (18 μm) – polyimide (PI, 75 μm) – Cu (18 μm) as fabrication substrate. (c)-(d) fPCB preparation, front (c) and back (d), via laser ablation process to define receiver coil, soldering pads, and via holes. (e) Fill via holes with silver paint to connect top and bottom electric traces. (f) Solder electronic components and μ-ILEDs using low temperature hot air soldering process. The number of μ-ILEDs can be further adjusted based on experimental requirements. (g) Encapsulate the entire device with chemical vapor deposited parylene (14 μm).

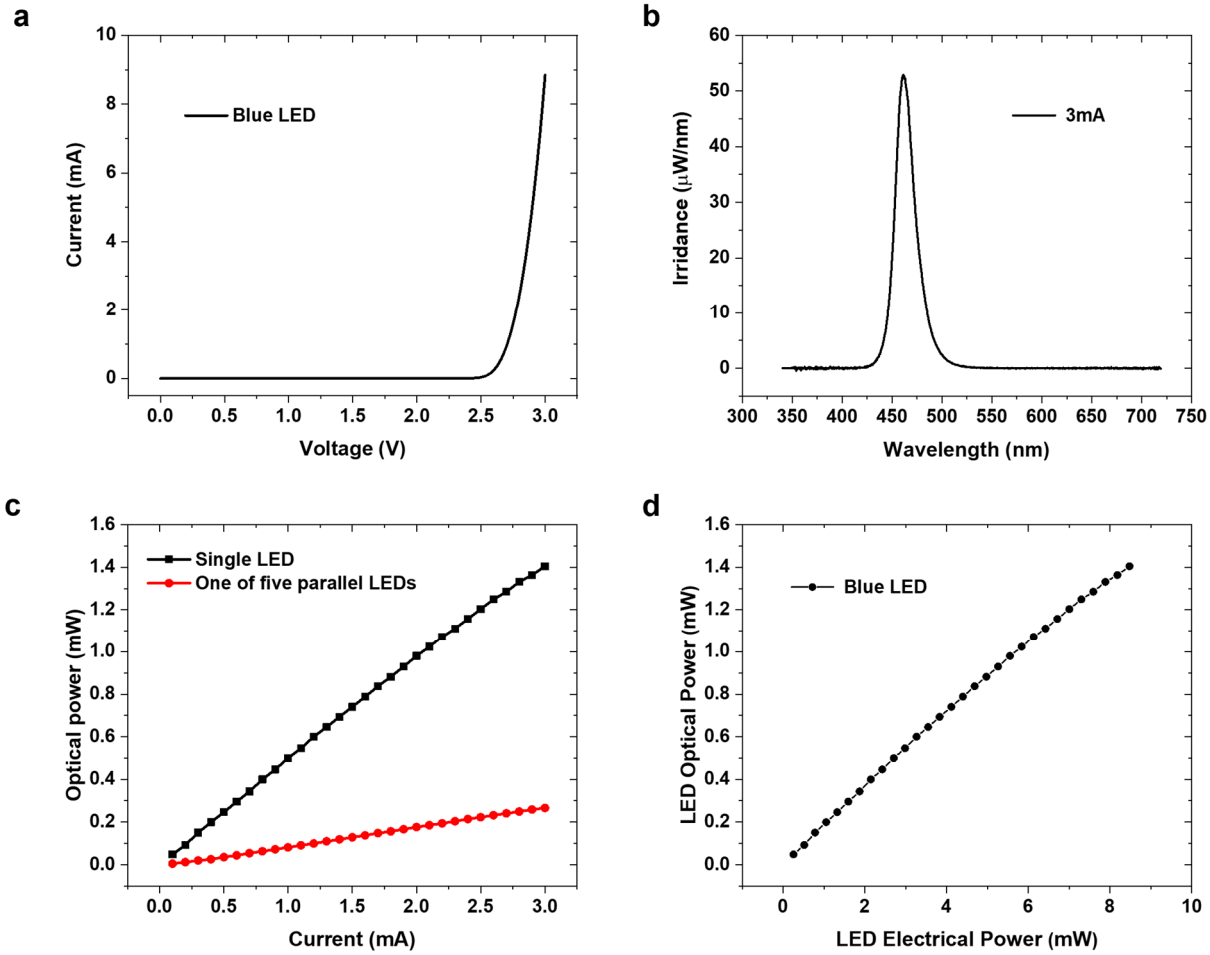

Fig. S3. μ-ILED characteristics. (a) μ-ILED I-V curves (460 nm). (b) Emission spectra of a μ-ILED driven at 3 mA. (c) Individual μ-ILED optical power with respect to total go-through current for passive optogenetic devices with single μ-ILED and one of five μ-ILEDs connected in parallel. (d) μ-ILED optical power vs. μ-ILED electrical power, which gives the working efficiency of 16.6%.

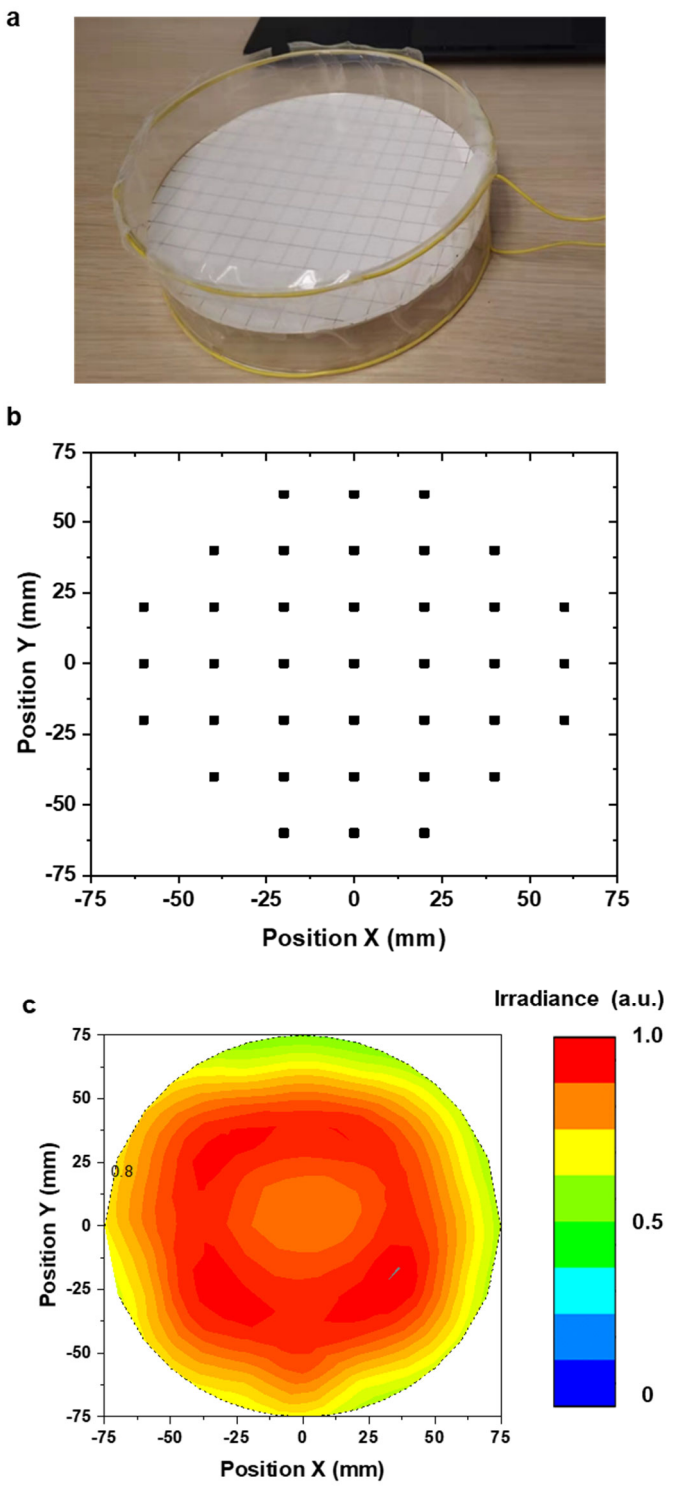

Fig. S4. Optical irradiance distribution. (a) Optical image of the antenna box with diameter of 150 mm. (b) The position of optical irradiance measurement in the antenna box. (c) The measured optical irradiance output intensity using passive optogenetic device with respect to the different locations as indicated in (b).

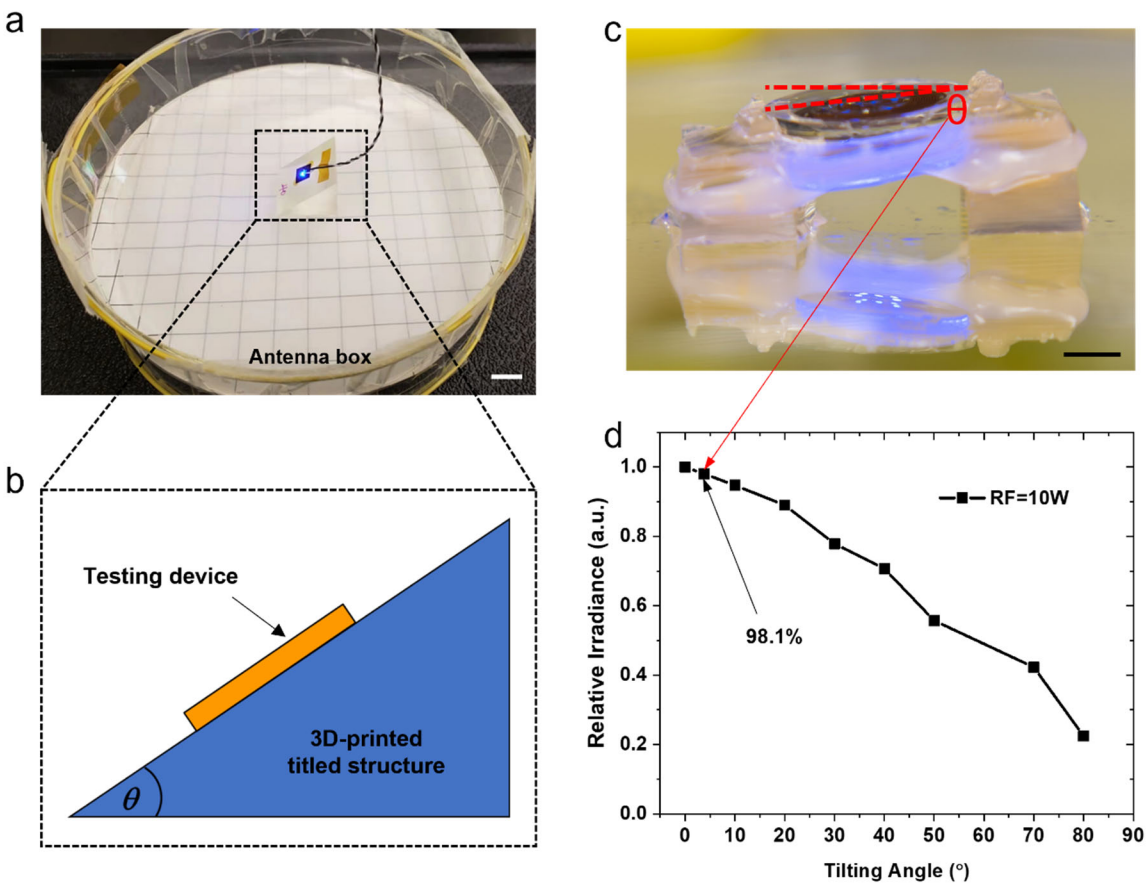

Fig. S5. Tilting effect on the optical irradiance output. (a) Photographic image of the experimental setup to study the device tilting effect by using a passive optogenetic device. (b) Schematic of the cross-sectional view of a testing device on a 3D-printed structure with a tilted angle θ. (c) Side view image of eBiobot. The tilted angle is 3.8 degrees based on the legs length mismatch and beam length. (d) Relative optical irradiance from a single μ-ILED with respect of tinting angle. Only 1.9% of irradiance loss occurred at 3.8 degrees. Scale bars: 1 cm for (a) and 2 mm for (c).

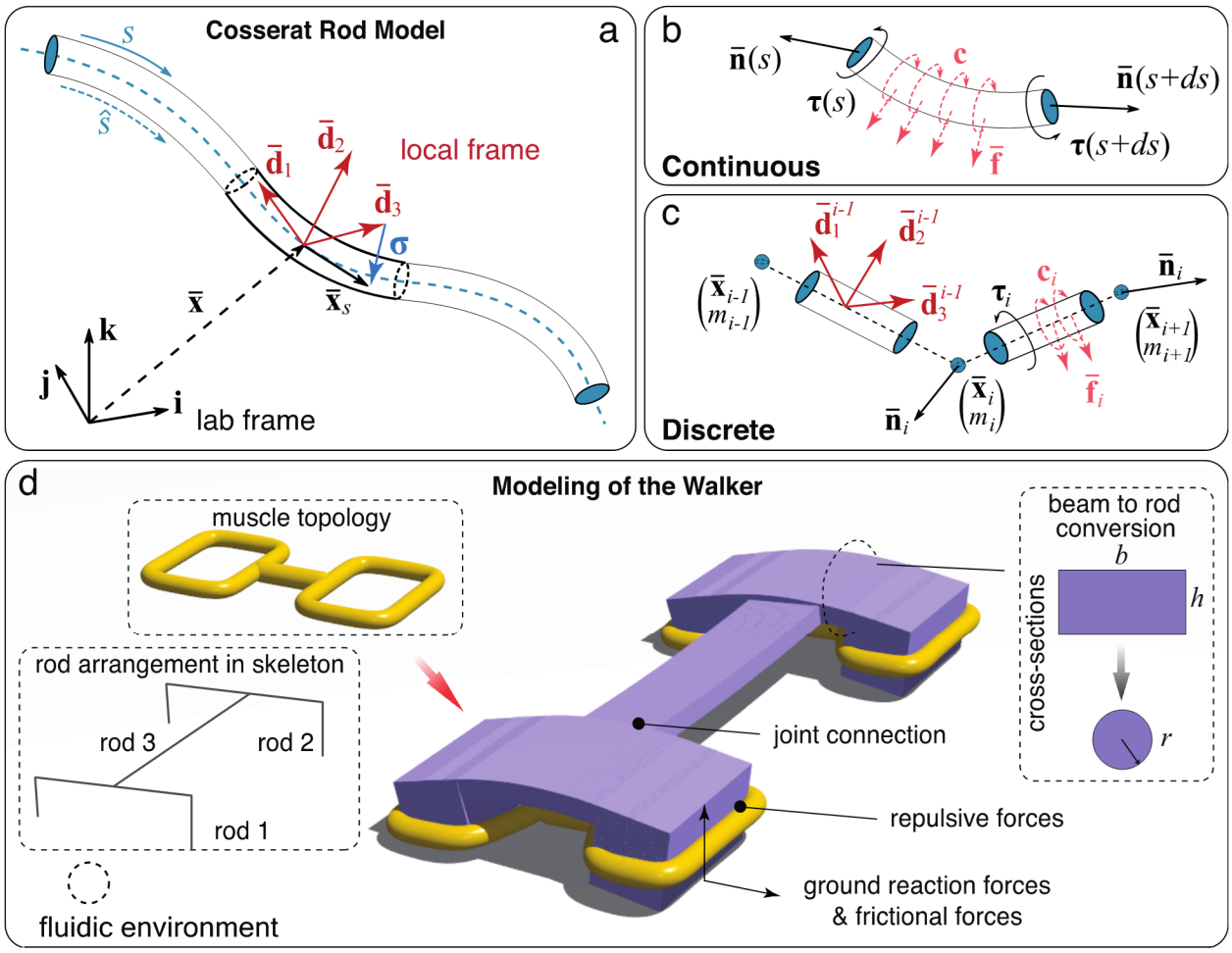

Fig. S6. Computational model of the eBiobot using Cosserat rods. (a) Schematic for the Cosserat rod model: A soft filament described by the centerline coordinates. Continuous (b) and discretized (c) model of a rod segment. (d) Each single eBiobot is modeled as an assembly of four Cosserat rods – one representing the scaffold and three representing the muscle tissue. The bipedal eBiobot is then constructed by incorporating two exact same single bots and connecting them using a straight rod. Rods are assembled into the walker using joint connection schemes. The walker is fully submerged in a fluidic environment and experiences reaction and frictional forces due to the contact with the ground.

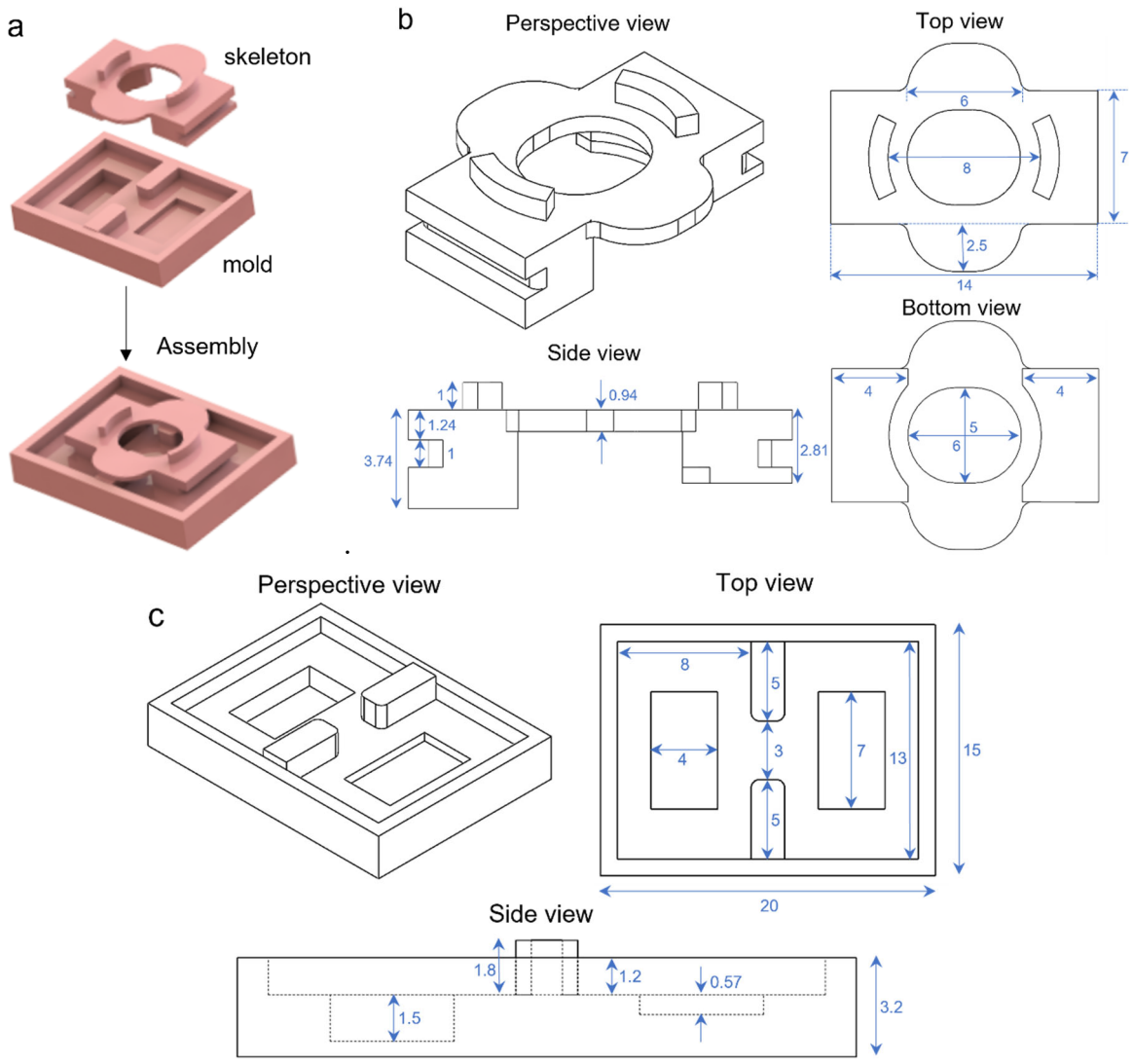

Fig. S7. Designs of 3D printed hydrogel structures for eBiobot. (a) Assembly of 3D printed skeleton and mold for eBiobot. CAD with dimensions of the final optimized generation (4^{th}) of (b) eBiobot skeleton and (c) its tissue seeding mold. The red circle in (b) indicates the inner radius of wireless optogenetics device. The width (3.5 mm) of central part in mold was considered to match with illuminations area of μ-ILEDs. Unit: mm.

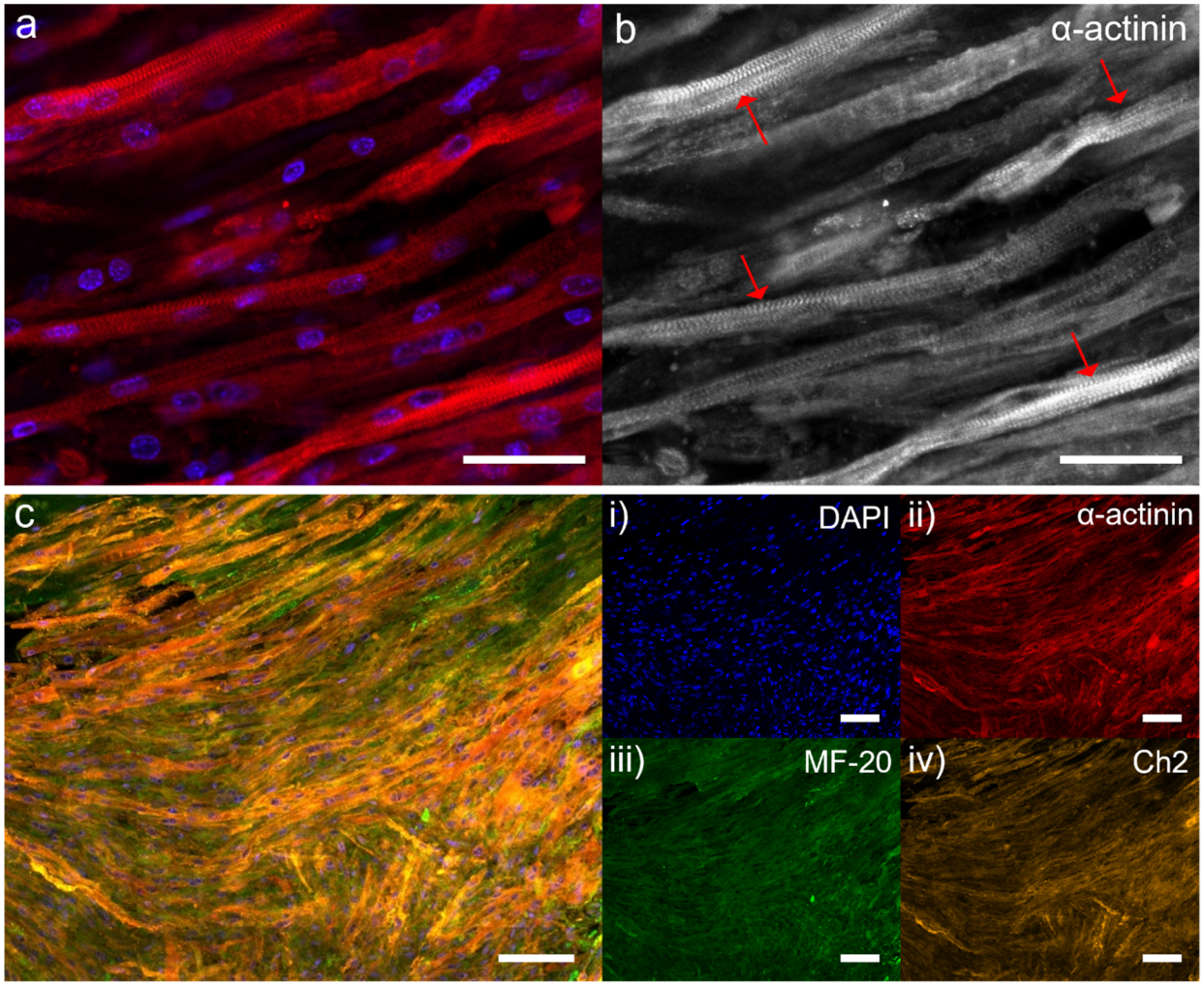

Fig. S8. Confocal immunostaining fluorescence images of muscle actuator. (a) Immunostaining fluorescence image of muscle actuator fixed on day 21 after differentiation showing aligned myotubes with α-actinin (red) and DAPI (blue) and (b) its α-actinin image to show cross-striations in myotubes. Red arrows indicate the aligned sarcomere bands. (c) Combined fluorescence image of muscle actuator with i) DAPI (blue), ii) α-actinin (red), iii) MF-20 (green), and iv) td-tomato tagged Channelrhodopsin-2 (orange). Scale bars: 50 μm for (a) and (b), 100 μm for (c) and (c)-i), ii), iii), and iv).

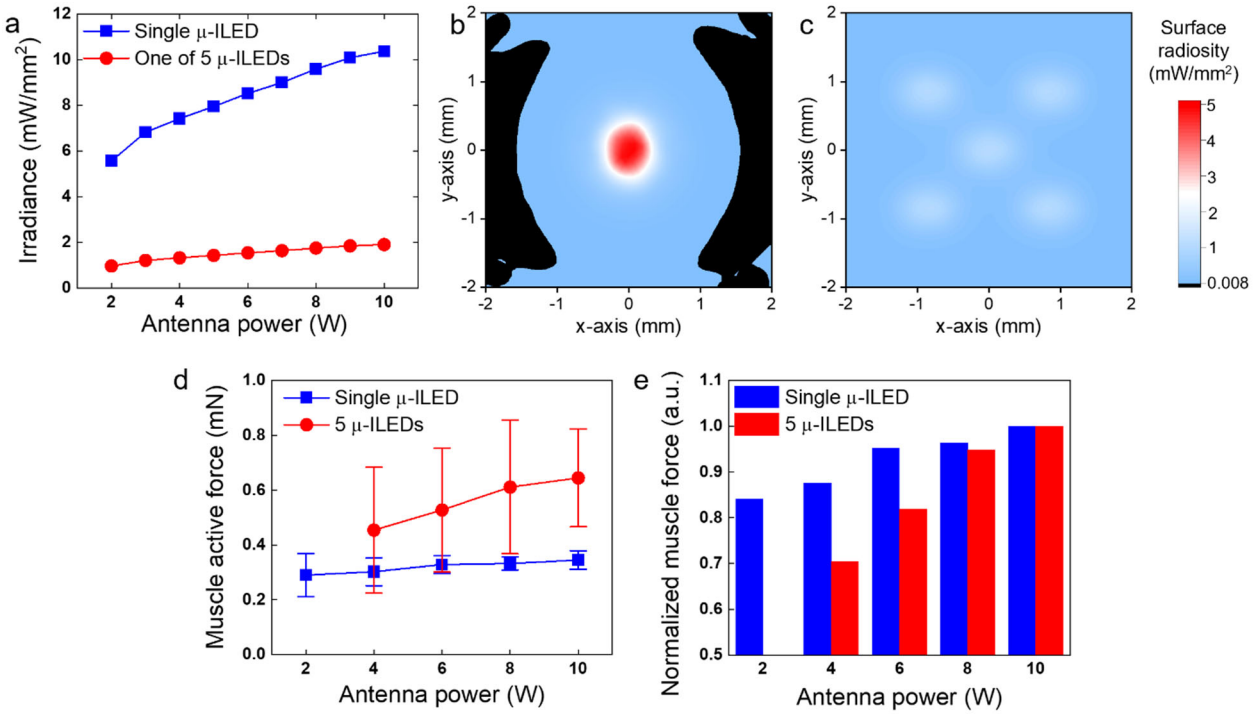

Fig. S9. Irradiance characteristics of wireless optogenetic devices with a single μ-ILED and 5 μ-ILEDs and respective muscle forces. (a) Light irradiance with respect to applied RF antenna power of (a) a single μ-ILED and one of 5 μ-ILEDs and surface radiosity on muscle actuator from (b) a single μ-ILED and (c) 5 μ-ILEDs at 10 W RF antenna power and 50 ms of pulse width. (d) Muscle active forces stimulated by a single μ-ILED and 5 μ-ILEDs with different RF antenna powers at 1 Hz and 50 ms pulse width and (e) their normalized muscle active forces by those stimulated by a single μ-ILED and 5 μ-ILEDs applied in 10 W and 50 ms of pulse width. The muscle twitching in 2W stimulated by 5 μ-ILEDs was not observed. Error bars correspond to the standard deviation from three measurements from three different samples.

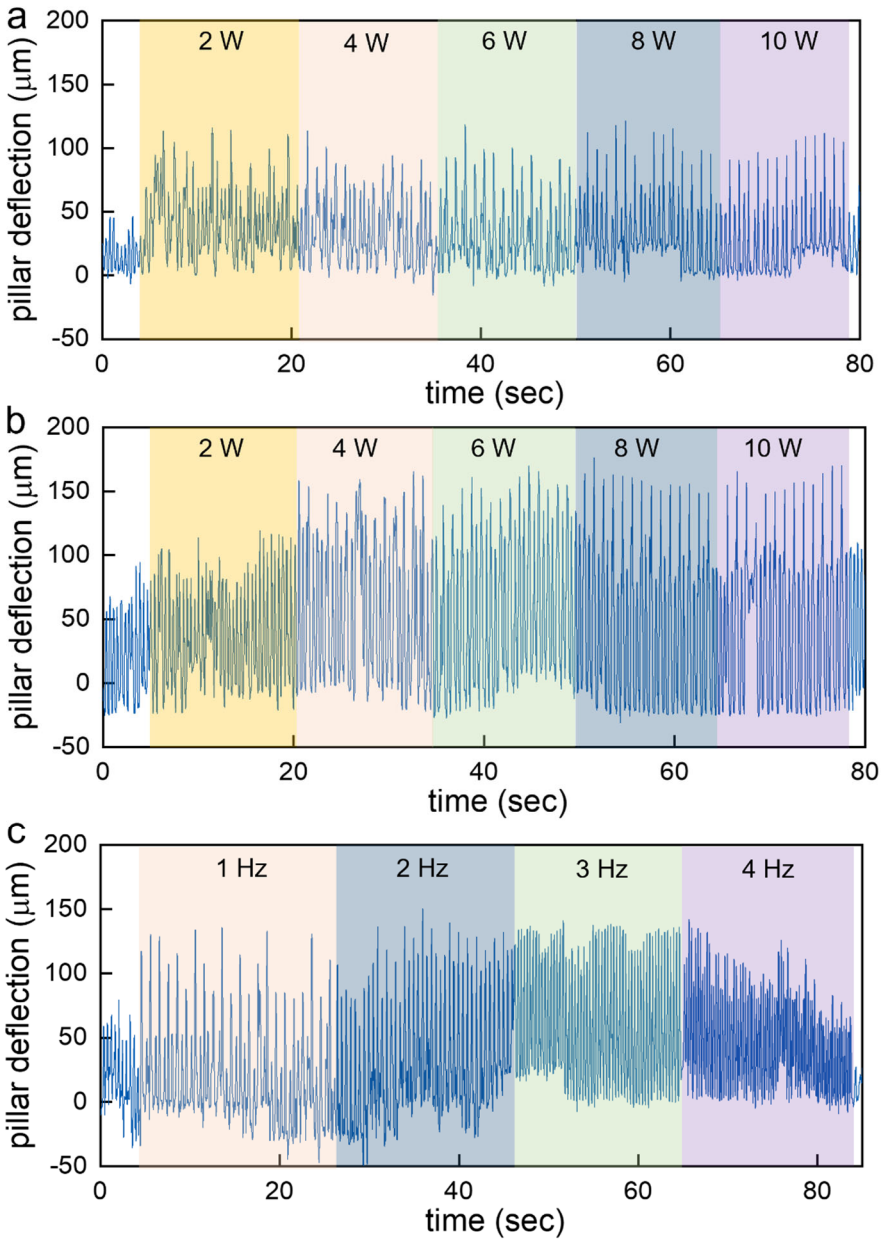

Fig. S10. Muscle actuations stimulated by a single μ-ILED and 5 μ-ILEDs. Pillar deflection-time curves of eBiobot stimulated by (a) a single μ-ILED and (b) 5 μ-ILEDs at 1 Hz, 50 ms pulse width and with different applied RF antenna powers and by (c) a single μ-ILED at different frequencies and 10 W RF antenna power.

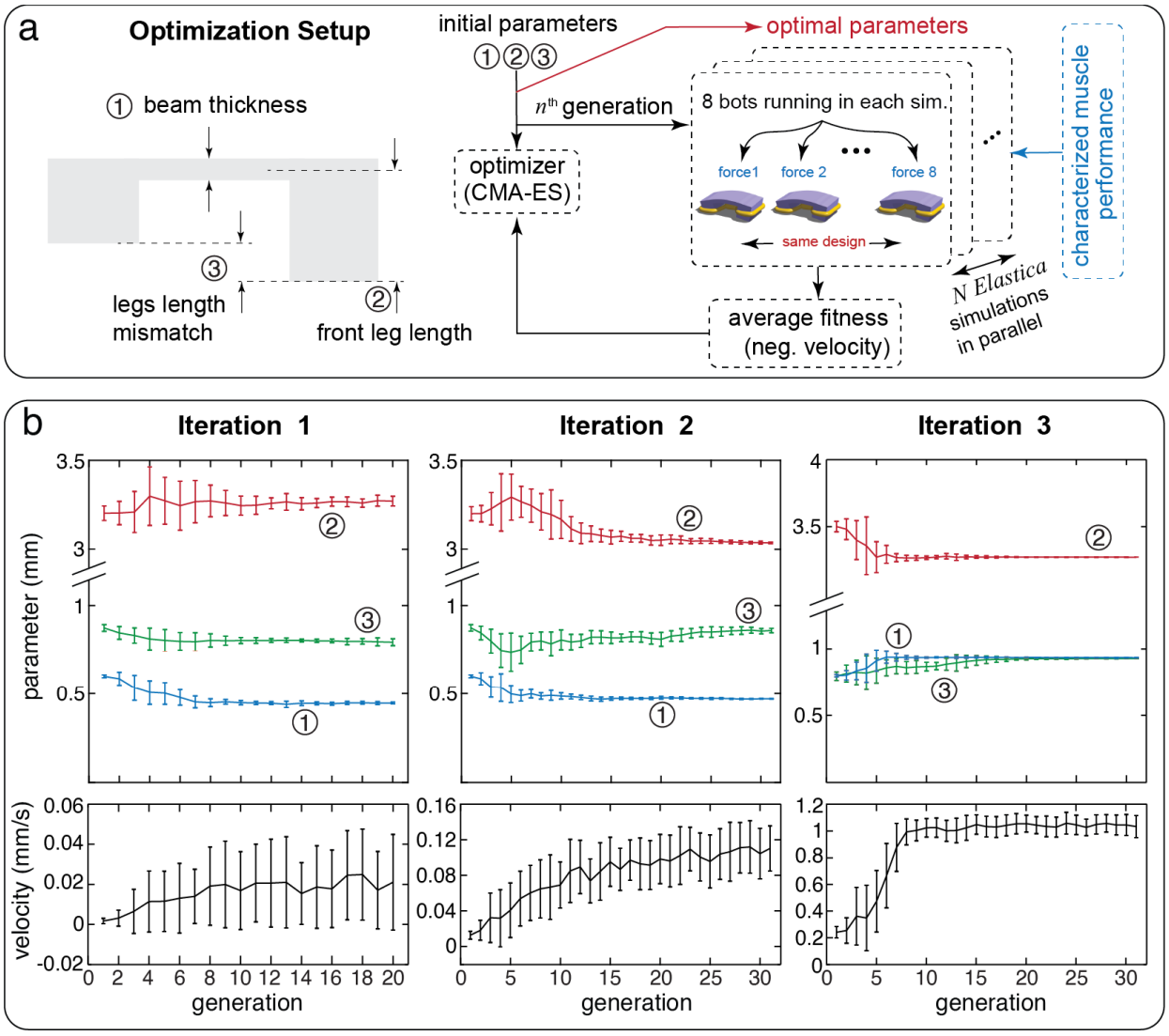

Fig. S11. Computational design optimizations. (a) Schematics for the design parameters and optimization course. (b) Result of three optimization iterations. In each optimization course, mean values of design parameters and resulting velocities (fitness) start to converge within 20 iterations. Error bars depict the standard deviations, resulted from the randomly sampled muscle force.

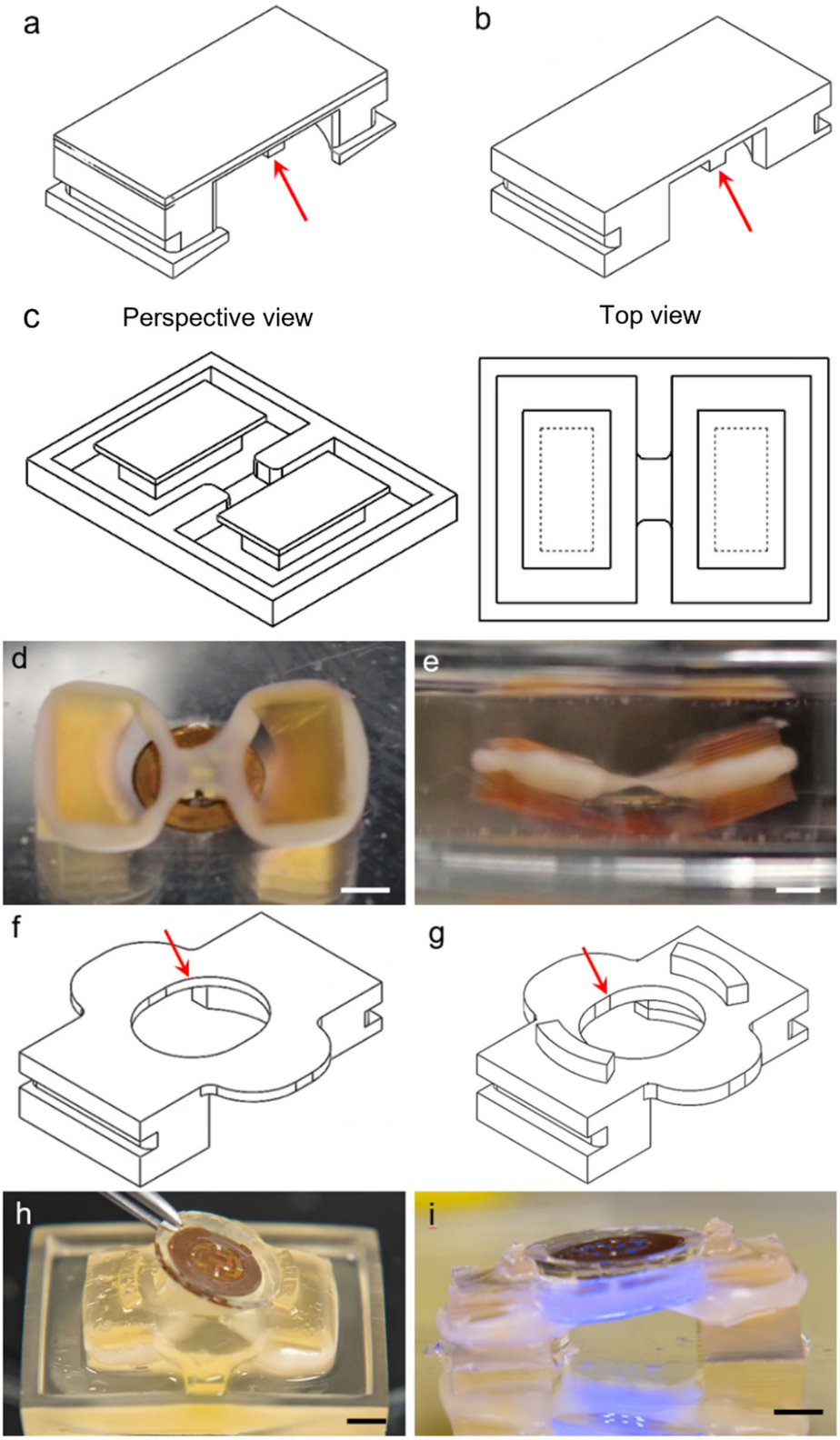

Fig. S12. Design iteration of eBiobot. CAD of skeletons for (a) 1st and (b) 2nd generations and (c) tissue seeding mold with dimensions for the 1st and 2nd generations. (d) Angled and (e) side views

images of eBiobot integrated with wireless optogenetic devices in the 2nd generation. CAD of (f) 3rd and (g) 4th skeleton generations and (h) angled and (i) side view images of eBiobot integrated with wireless optogenetic devices in the 4th generation. The 1st design was selected from the previous study (*9*) and dimensions have been changed through the evolutionary computational optimizations. From the 3rd generation, wireless optogenetic devices were integrated on the top of skeleton after attaching on PDMS substrate, while they had been integrated inside of the beam on the stage using glue in 1st and 2nd generations. In the 4th generation, the printed stoppers were added to prevent the optogenetic device from slipping as overserved in the 3rd generation. Red arrows indicate the locations to integrate wireless optogenetic devices. Scale bars: 2 mm.

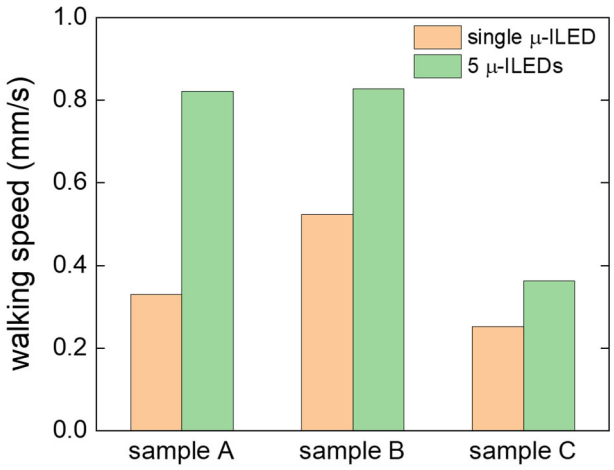

Fig. S13. Walking speeds comparison for eBiobots stimulated by a single or 5 μ-ILEDs. Walking speeds of eBiobots stimulated at 4 Hz, 50 ms pulse width, and 10 W RF antenna power and by a single μ-ILED or 5 μ-ILEDs for three samples in movie S6.

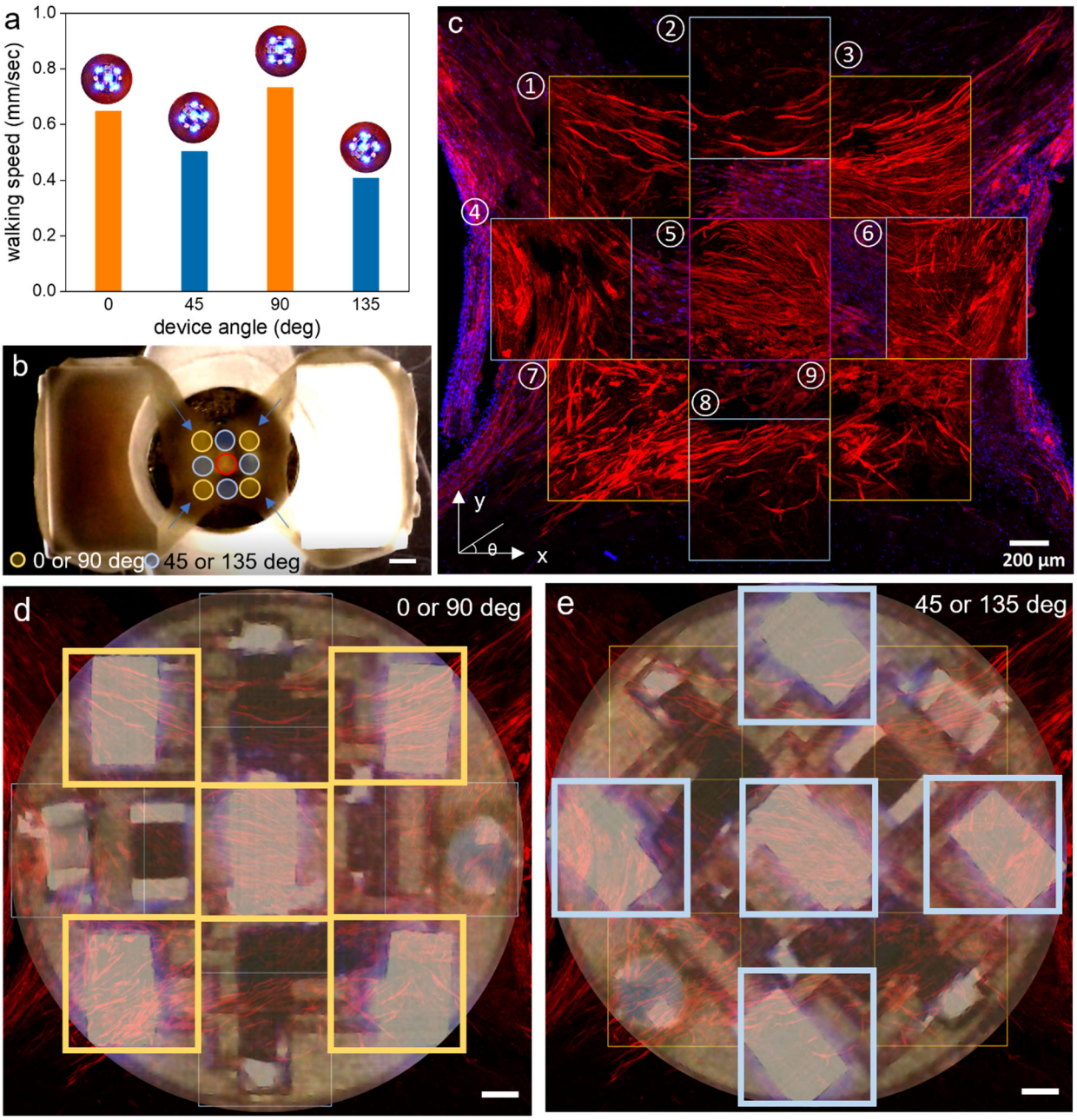

Fig. S14. Different walking speeds depending on the orientation of 5 μ-ILEDs. (a) Walking speeds of eBiobot with different rotating angles of 5 μ-ILEDs on skeleton beam in movie S7. (b) The illumination region of 5 μ-ILEDs on the eBiobot muscle actuator. The yellow, blue, and red circles indicate the illumination areas in 0 or 90 degrees, 45 or 135 degrees, and all cases, respectively. (c) Confocal immunostaining tile image of the central part of muscle actuator stained with α-actinin as red and DAPI as blue. The axis and angle in left bottom and its numbers for squares correspond to the myotubes alignments analysis in fig. S15-17. Overlapped images with the 5 μ-ILEDs and fluorescence image with α-actinin of the central part of muscle actuator in wireless optogenetic device angles with (d) 90 and (e) 135 degrees. Scale bars: 1 mm for (b) and 200 μm for (c)-(e).

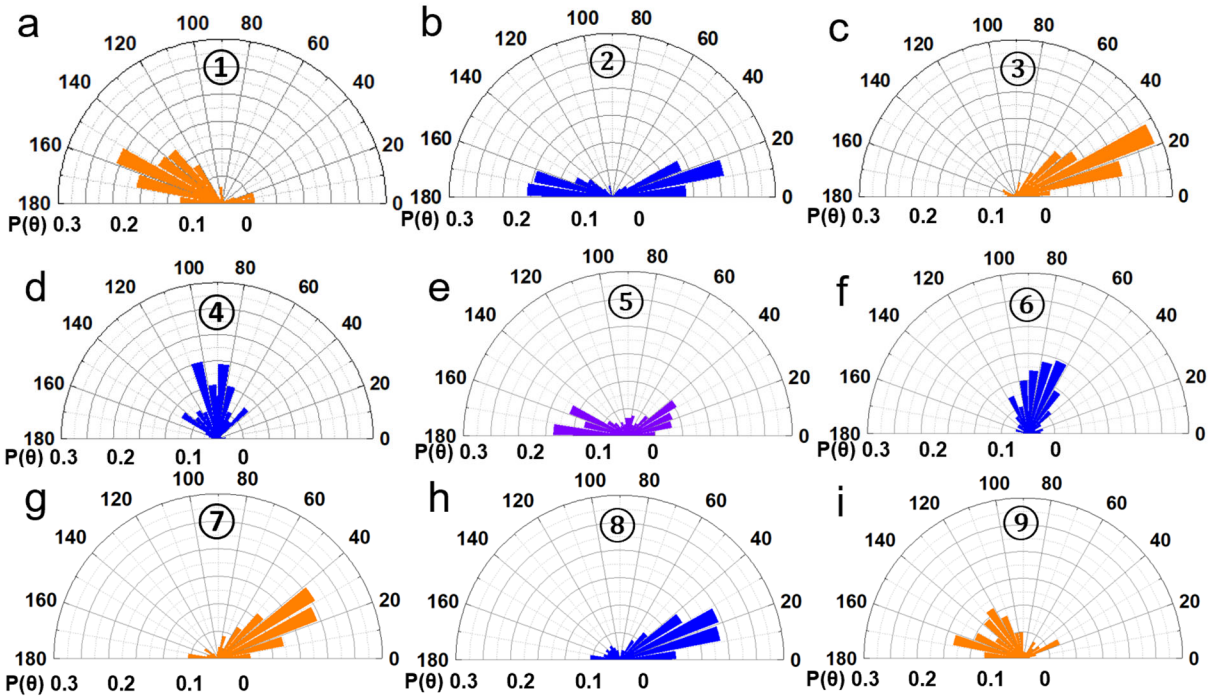

Fig. S15. Myotubes orientations analysis of muscle actuator. Polar histograms of α-actinin-stained myotubes alignments from 3 samples in regions for (a) ①, (b) ②, (c) ③, (d) ④, (e) ⑤, (f) ⑥, (g) ⑦, (h) ⑧, and (i) ⑨ corresponding with fig. S14 (c).

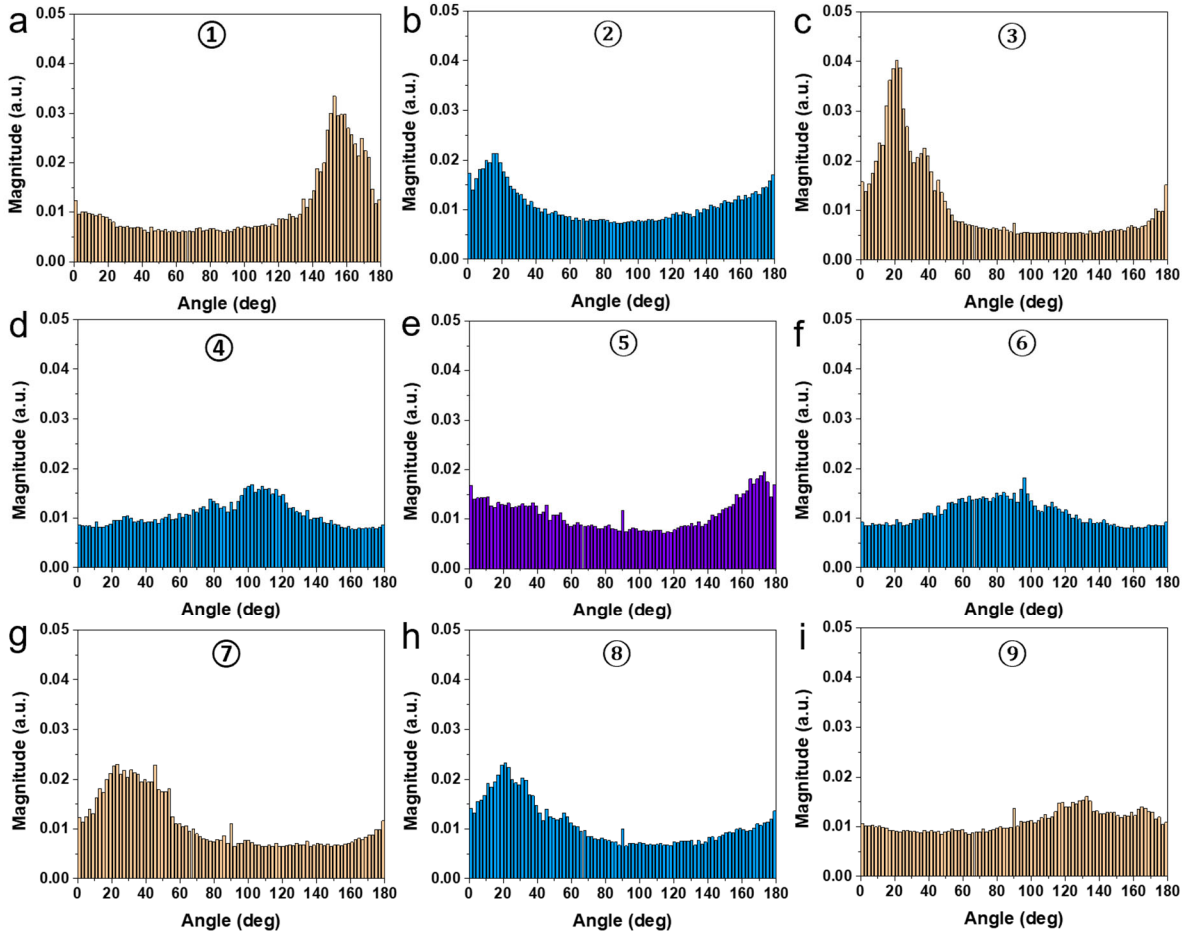

Fig. S16. FFT analysis for myotubes alignment of muscle actuator. FFT analysis of α-actinin-stained regions for (a) ①, (b) ②, (c) ③, (d) ④, (e) ⑤, (f) ⑥, (g) ⑦, (h) ⑧, and (i) ⑨ corresponding with fig. S14 (c).

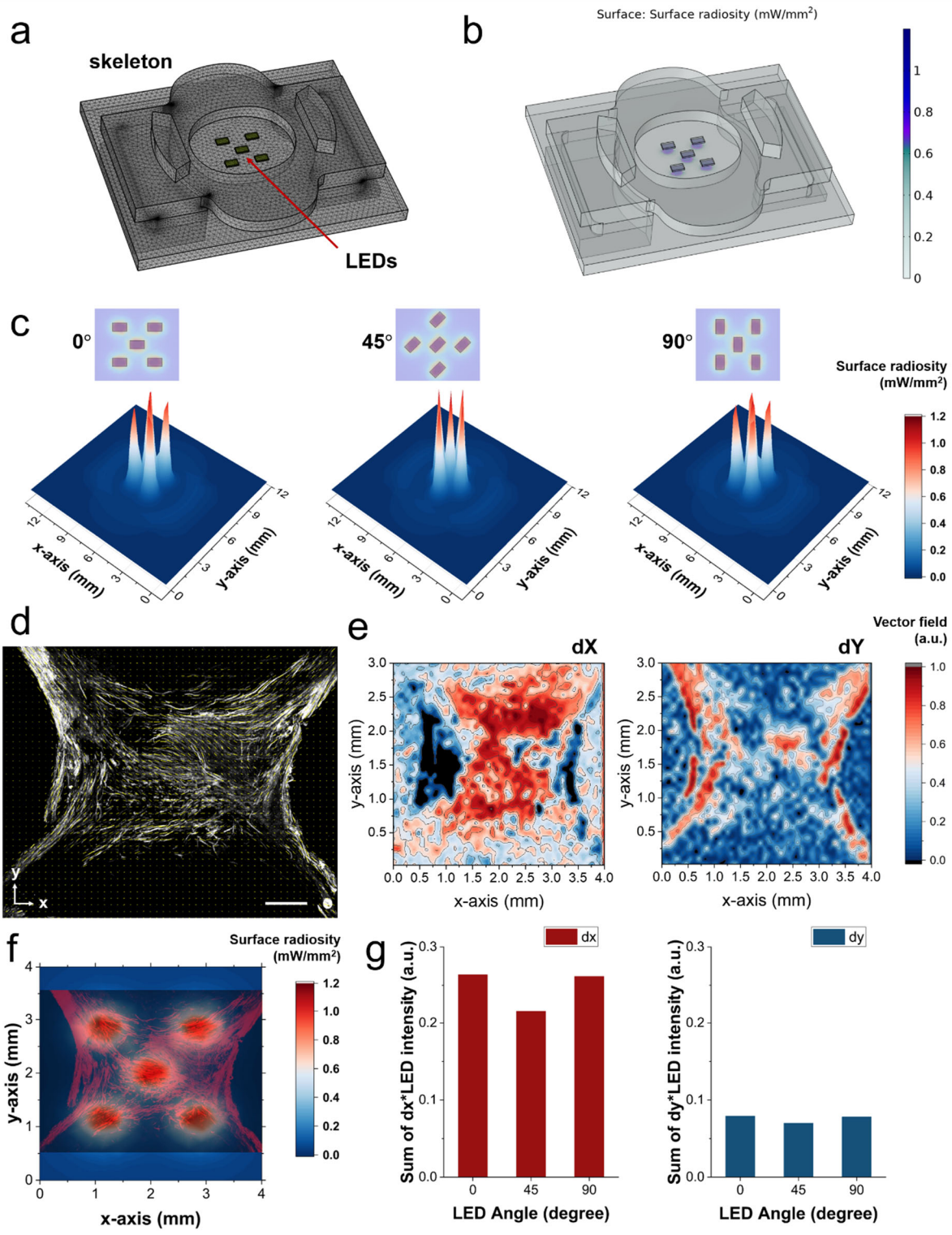

Fig. S17. The numerical prediction of locomotion of eBiobot corresponds to the different configurations of 5 μ-ILEDs. (a) Finite-element mesh used for COMSOL® simulation. (b) The radiation of 5 μ-ILEDs on a muscle actuator. (c) Surface radiosity on a muscle actuator with

different configurations of 5 μ-ILEDs (0, 45 90 degrees rotating). (d) Visual directional analysis of myotubes alignments from fig. S14 (c). The orientation of the vector field is evaluated according to the structure tensor computation in ImageJ software. Scale bar: 500 μm. (e) Visualization of the vector field of myotubes alignments in x- (dX) and y-axis (dY). The vector field distribution has similar spatial trends with myotubes alignments analysis in fig. S15 and S16. (f) Alignment of optical images of myotubes and the distribution of radiosity of 5 μ-ILEDs. The locomotion factor of 5 μ-ILEDs radiated eBiobot is calculated by multiplying the vector field of myotubes in x- and y-axis by the radiosity of 5 μ-ILEDs with different configurations for each pixel. (g) Bar plot of the sum of locomotion factors for every pixel in x- and y-axis corresponds to 0, 45, and 90 degrees of 5 μ-ILEDs.

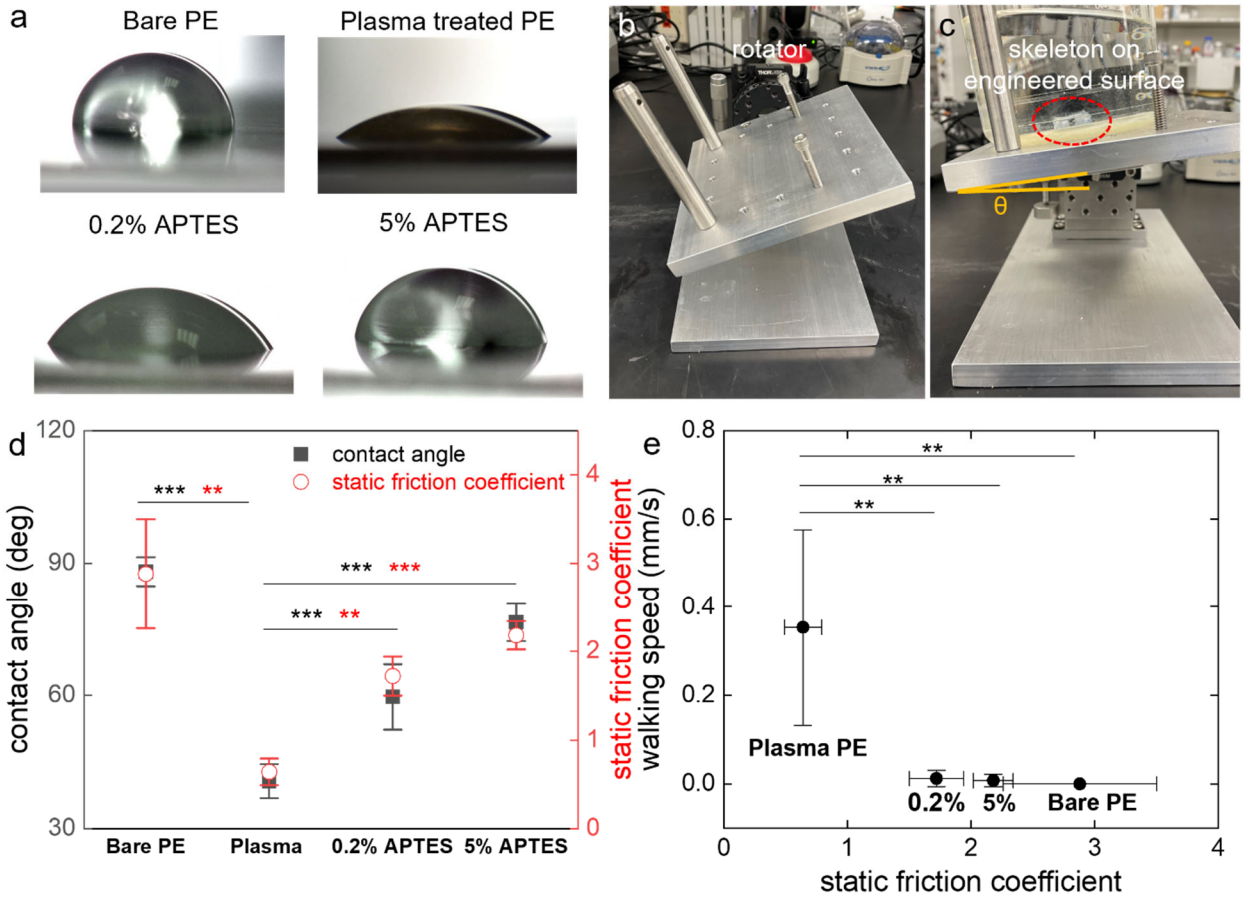

Fig. S18. Friction study of engineered surfaces for improved walking performance of eBiobot. (a) Side microscopic images for water drop on engineered polyethylene (PE) film. Images of (b) customized angle of repose measurement system with the rotator and (c) how to measure the sliding angle. (d) Contact angle (black) and static friction coefficient (red) of engineered PE surfaces. (e) Walking speeds of eBiobots on engineered PE surfaces with their static friction coefficient ranges (Plasma treated, 0.2% and 5% APTES treated, bare PE surfaces from the left). Error bars correspond to the standard deviation of 5 measurements for contact angle and minimum 3 for static friction coefficient and 6 measurements for walking speed. Statistical significance: *P < 0.05, **P < 0.01, ***P<0.001. Black and red asterisk in (d) correspond to statical significance of contact angle and static friction coefficient, respectively.

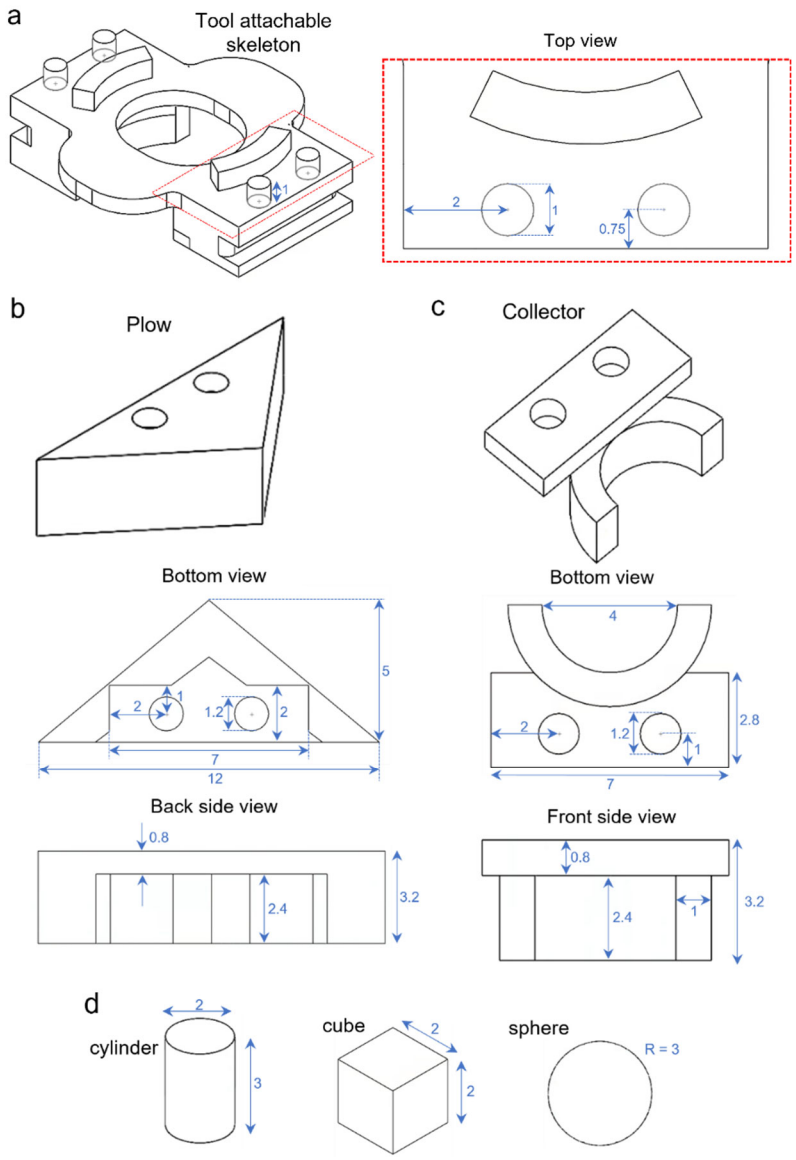

Fig. S19. Designs of tool attachments for functional eBiobot using Lego® like assembly. CAD with dimensions for (a) tool attachable skeleton for functional eBiobot, (b) plow, (c) collector, and (d) obstacles used in Fig. 5, movie S8 and S9. Units: mm.

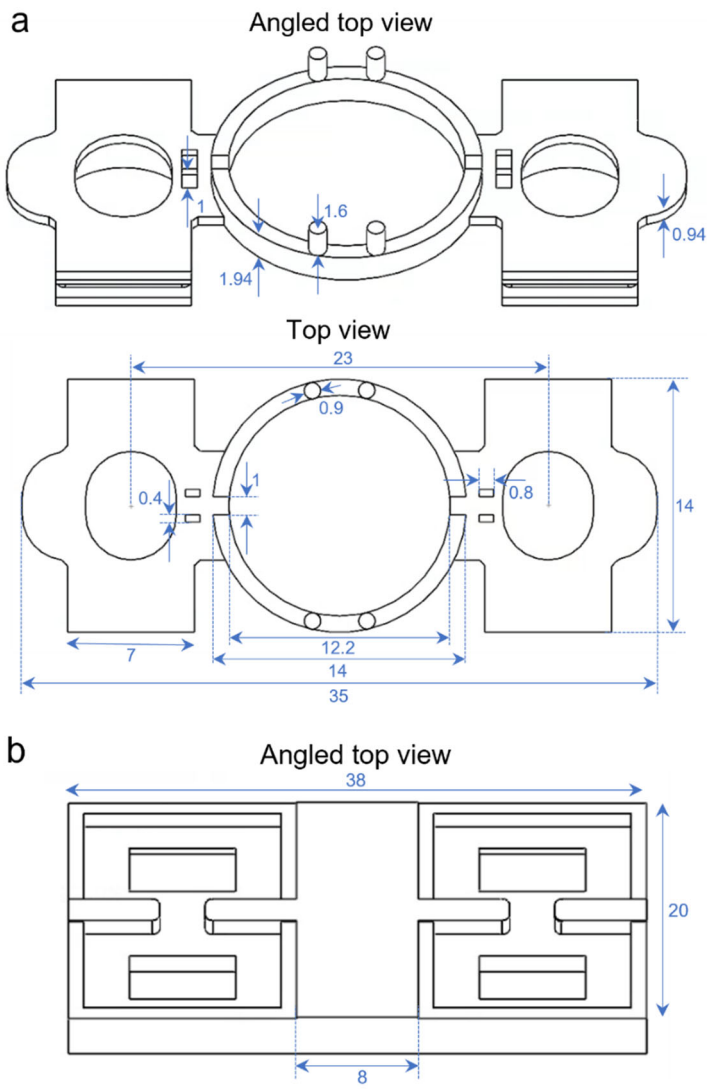

Fig. S20. Designs of 3D printed parts for bipedal eBiobot. CAD with dimensions of (a) bipedal eBiobot skeleton and (b) its tissue seeding mold. Units: mm.

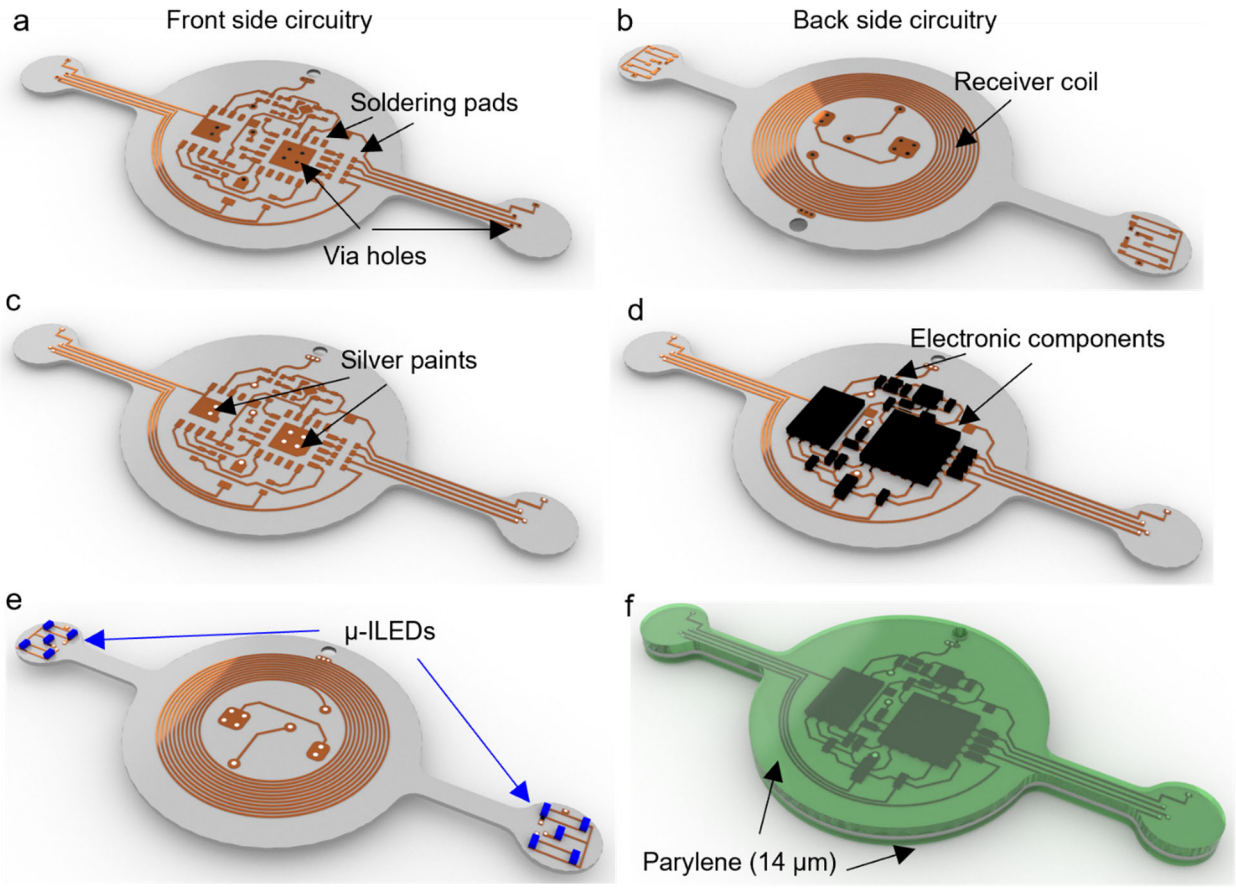

Fig. S21. Fabrication process for μC-contained wireless optogenetic devices that power bipedal eBiobots. (a)-(b) Apply aligned laser ablation process on front (a) and back (b) surfaces of a tri-layer flexible printed circuit board (fPCB) composed of Cu (18 μm) – polyimide (PI, 75 μm) – Cu (18 μm) to define receiver coil, soldering pads, and via holes. (c) Fill via holes with silver paint to connect top and bottom circuitry. (d)-(e) Apply hot air soldering to mount electronic components (d) and μ-ILEDs (e) on designated locations. The number of μ-ILEDs can be further adjusted based on experimental requirements. (f) Encapsulate the entire device with chemical vapor deposited parylene (14 μm).

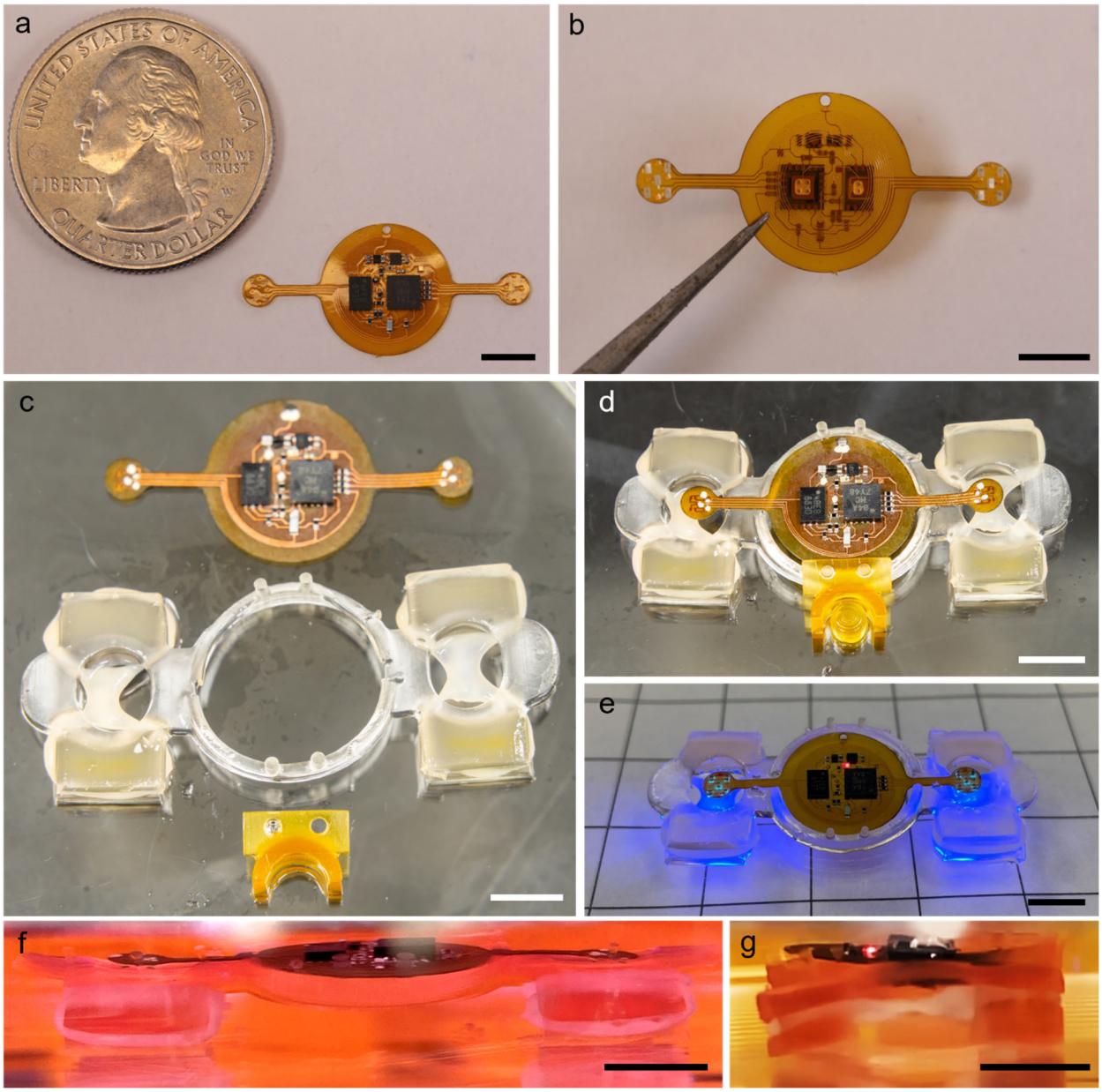

Fig. S22. Photographic images of μC-contained wireless optogenetic device and its assembly with bipedal eBiobot. Images for (a) top view and (b) bottom view of **μC-contained**wireless optogenetic device and (c) before and (d) after assembly of electronics with bipedal eBiobot and collector (e) with light illuminations from μ-ILEDs. Images of bipedal eBiobot's (f) front view and (g) side view. All scale bars: 5 mm.

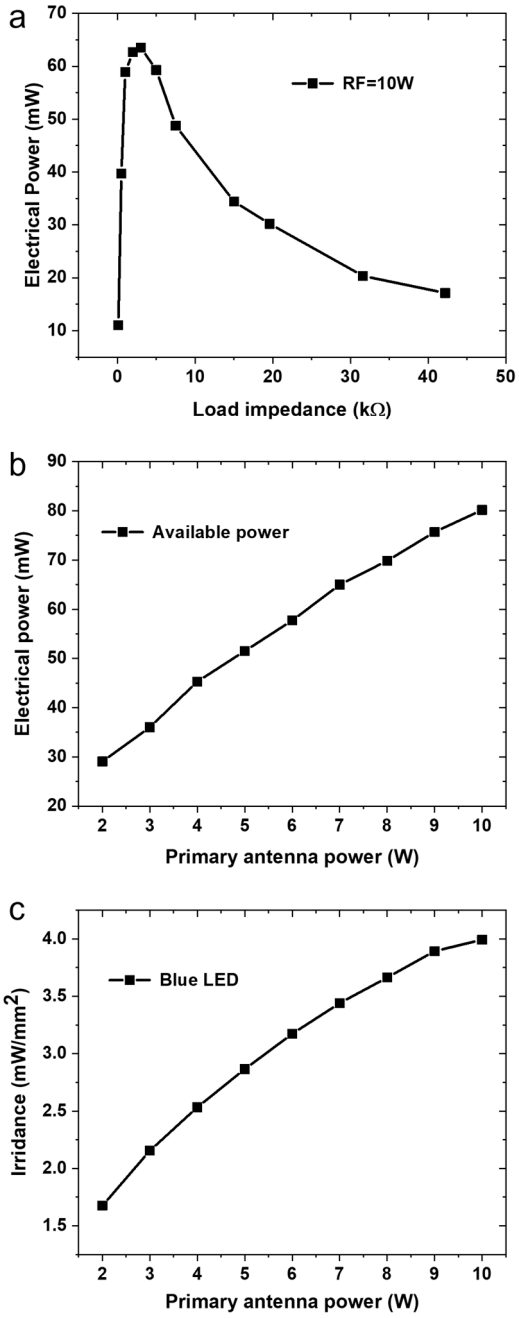

Fig. S23. Electrical and optical characterizations of μC-contained wireless optogenetic device with dual panels of μ-ILEDs. (a) Electrical power supplied to the dual-panel optogenetic device as a function of loading impedance at 10 W RF antenna power. (b) Maximum total harvested power for the dual-panel optogenetic device as a function of RF transmission antenna power. (c) optical irradiance output of one μ-ILED, out of ten simultaneously activated, driven by the dual-panel optogenetic device as a function transmission antenna power.

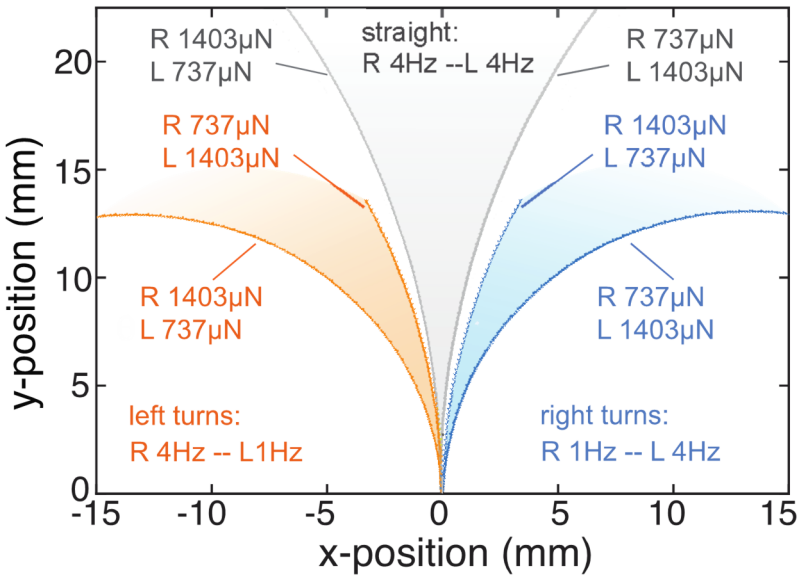

Fig. S24. Parameters used in simulation for predicting the turning capability and robustness of the bipedal eBiobot. R and L denote frequencies or forces set for right or left leg, respectively. The frequency settings determine whether the bot will walk straight or turn, while the force offsets between the two legs define the trajectory envelope of each moving mode. 737μN and 1403 μN forces are the lower and upper bounds of the muscle force range characterized during the last design iteration and utilized here for the prediction.

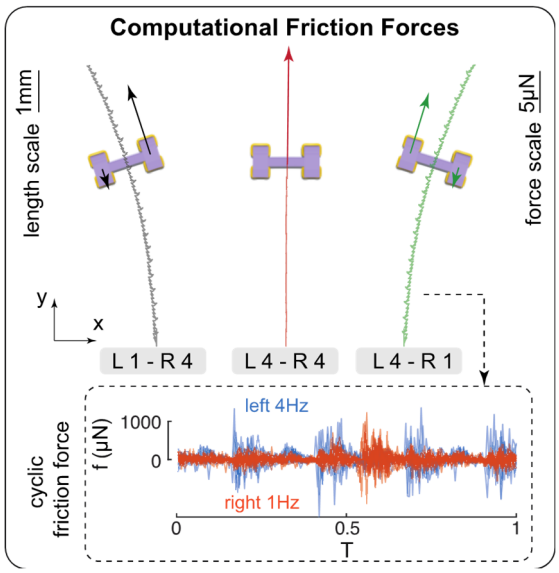

Fig. S25. Analysis of frictional forces at the leg-substrate interface. Traction forces due to frictional effects are computed using our numerical bipedal walker model. Each side of the walker skeleton makes contact with the substrate through front and rear legs. Due to the length mismatch between the two legs, asymmetric frictional forces are generated at the interface, resulting in a periodic net traction force over each cycle. We numerically compute this net force at each side of the bipedal walker, and plot the magnitude and direction of the force in correspondence with the bipedal eBiobot's center trajectory (forces are averaged over 15s of simulation). Under differential stimulation, where one side is stimulated by 4 Hz and the other side by 1 Hz, a traction force mismatch is found between the two sides, causing the turning motion of the walker. Moreover, the overall friction force of the walker (sum of both sides) under symmetric stimulation (4 Hz on each side) points straightly to the front direction of the walker, with its magnitude roughly twice of the overall forces in the turning cases. We also plot here the instantaneous net force at each side of the walker under differential stimulation (curves from 15 cycles are overlaid in the plot), illustrating how the net forces changes in corresponding to each muscle contraction. Due to the buoyancy, the bipedal eBiobot doesn't always make firm contact with the substrate at all legs, hence the high force fluctuation in the plot.

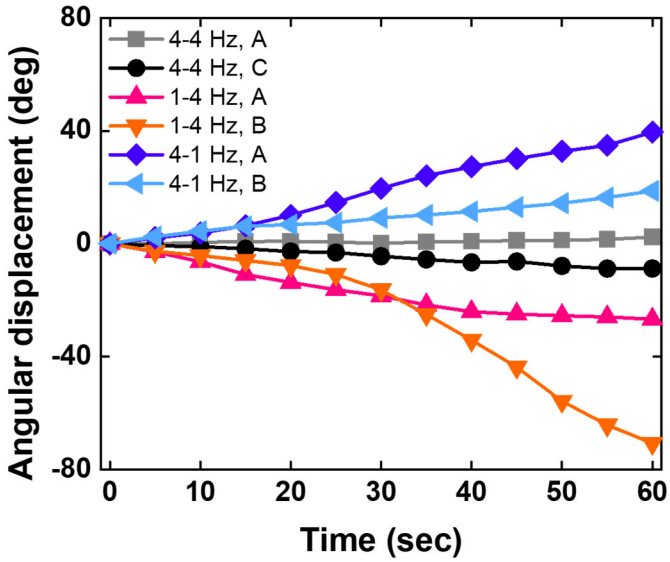

Fig. S26. Angular displacements for turning or straight walking bipedal eBiobots. Angular displacement vs. time curves for bipedal eBiobots with different stimulation schemes from Fig. 6 (E), (F) and movie S11.

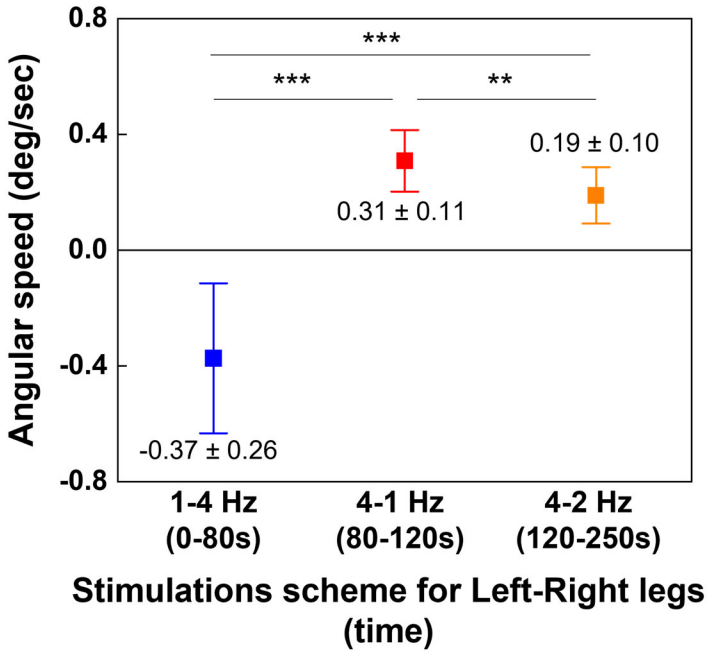

Fig. S27. Angular speeds depending on modulations scheme. Angular speeds of turning bipedal eBiobot in Fig. 7 (C) and movie S14 for every 5 seconds with different stimulations scheme. Positive angular speeds mean turning to clockwise side, while negative means turning to counterclockwise side. Error bars correspond to the standard deviations of calculated angular speeds for every 5 seconds in a turning bipedal eBiobot. (Mean ± standard deviation). Statistical significance: **P < 0.01, ***P<0.001.

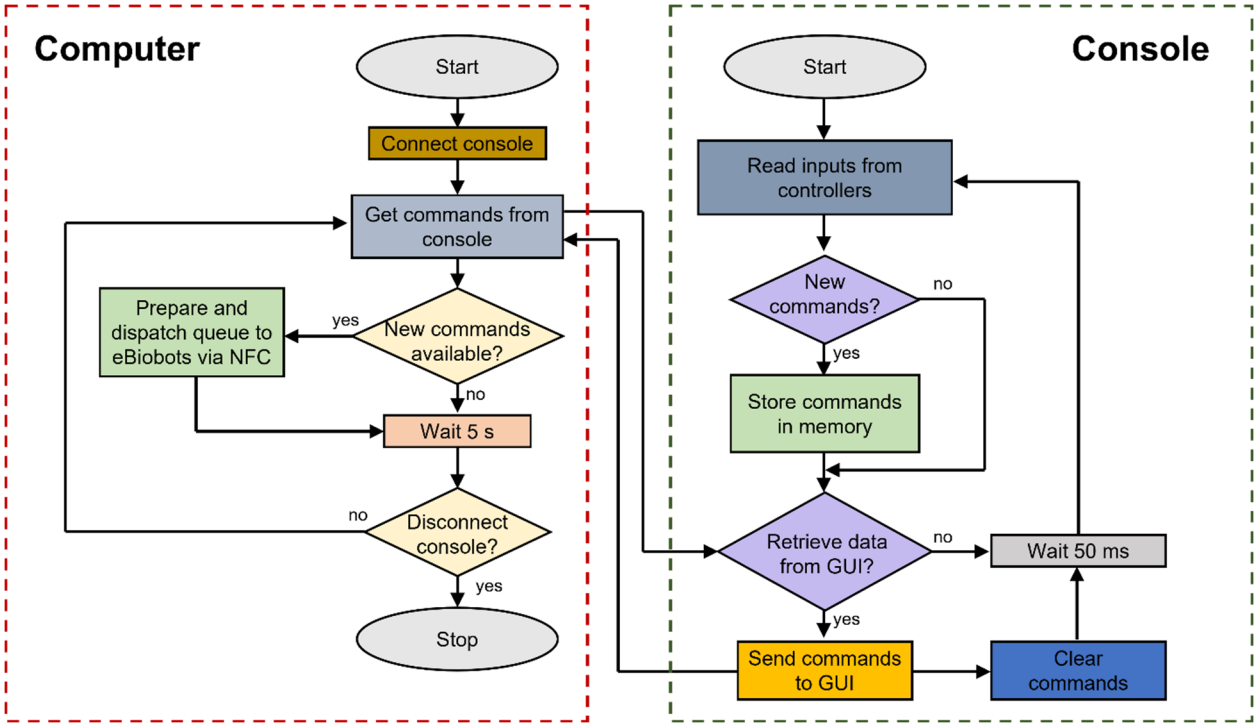

Fig. S28. Logic diagram that depicts the operation of the console. The software running in the computer controls a temporized event to interrogate the console and retrieve the commands issued by the users on each of the 6 remote controllers. If new commands are reported, then the GUI dispatch the control commands to the corresponding eBiobot.

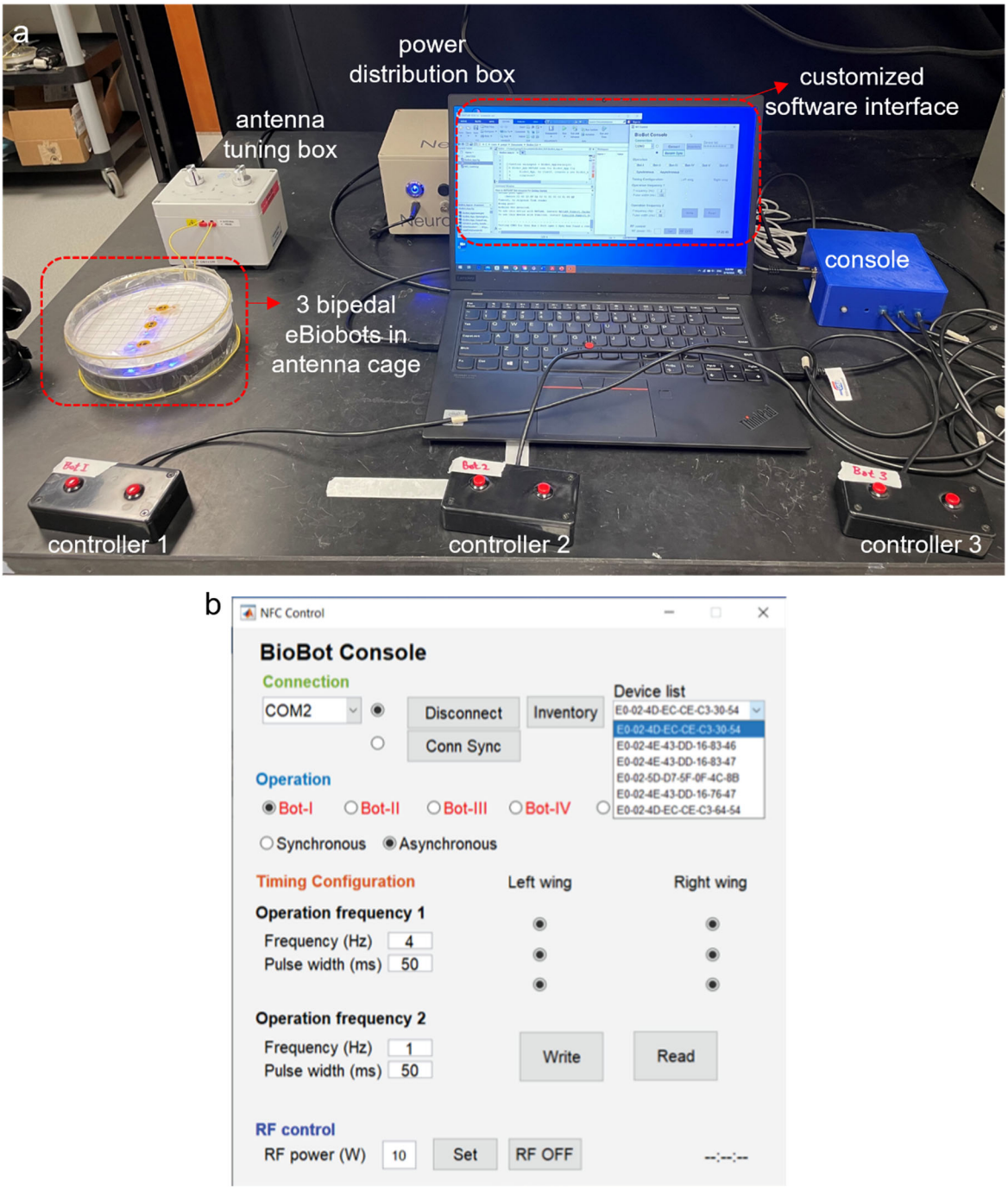

Fig. S29. Set up for individual remote control of multiple eBiobots with gaming controllers. (a) Experimental setup image for individual remote control of multiple bipedal eBiobots using the console system connected with multiple gaming controllers, customized software, and antenna setup. (b) Software interface for console operation.

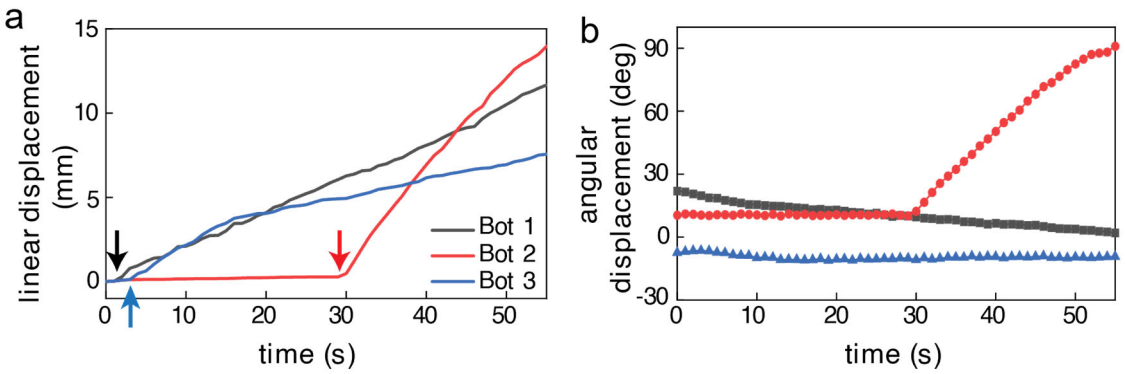

Fig. S30. Individual remote control of three bipedal eBiobots. (a) Linear and (b) angular displacement vs. time curves for eBiobots 1, 2, and 3 from Fig. 3(e)-iii, iv. Arrows indicate when gaming controllers start operations.

Table S1. Walking speeds of different generations of eBiobots. Walking speeds of eBiobots with different design iterations stimulated by 1 or 5 μ-ILEDs measured by three different samples. In the 1st generation, only single μ-ILED was used. The experimental results of Fig. 3 are plotted as average from walking samples.

Generations	**1st**		**2nd**		**3rd**		**4th**	
# of LEDs	**1**	**5**	**1**	**5**	**1**	**5**	**1**	**5**
Walking speeds from 3 different samples	0.04	-	0.02	0.25	0.25	0.41	0.33	0.82
	Not Walk	-	0.03	0.07	0.03	0.36	0.52	0.83
	Not Walk	-	Not Walk	Not Walk	Not Walk	Not Walk	0.25	0.36
Average ± STDEV	0.04	-	0.02	0.16	0.14	0.39	0.37 ± 0.14	0.67 ± 0.27

Table S2. Locomotion comparisons with previous biohybrid robots. Locomotion mechanisms, actuation type, body length, and maximum speeds, speeds with body length per second for previous biohybrid robotics systems and surface type for biohybrid robotic walkers. The eBiobots in this work recorded the fastest speed among biohybrid robotic walkers or skeletal muscle-based bio-hybrid robots including swimmer. The bipedal eBiobot in movie S12 showed 1.75 mm/sec of walking speed, another recording the fastest walking speed with the largest body scale among all bio-hybrid robotics systems.

Mechanism	**Actuator type**	**Body length (mm)**	**Maximum speed (mm/sec)**	**Speed (body length/sec)**	**Surface for walker**	**References**	
Swimmer	Cardiomyocytes	6	0.4	0.067	N/A	Feinberg et al. (*33*)	
		6	2.4	0.4		Nawroth et al. (*34*)	
		1	0.081	0.081		Williams et al. (*35*)	
		16.3	3.2	0.2		Park et al. (*5*)	
		14	15	1.1		Lee et al. (*6*)	
	Neuromuscular junction driven 3D skeletal muscle	3.2	0.0007	0.00022		Aydin et al. (7)	
	3D Skeletal muscle	12	0.79	0.066		Guix et al. (*11*)	
Walker	Cardiomyocytes	0.4	0.038	0.095	Petri dish	Xi et al. (*36*)	
		2	0.1	0.05		Kim et al. (*37*)	
		7	0.24	0.034		Chan et al. (*15*)	
	3D skeletal muscle	6	0.16	0.027		Cvetkovic et al. (*29*)	
		14	0.5	0.036		Pagan-Diaz et al. (9)	
		14	0.83	0.059	O_2 plasma treated PE	This work	movie S4
		35	1.75	0.05			movie S12

Table S3. *Elastica* simulation parameters. List of parameters utilized in the modeling and simulation of the eBiobot.

Parameters	Values	Parameters	Values
Time step	2.5×10^{-7} s	Simulation time	$20 - 60$ s
Number of elements in scaffold	30	Number of elements in muscle	32
Scaffold Young's modulus	270 kPa	Muscle Young's modulus (*38*)	10 kPa
Scaffold density	$1.12\ \mathrm{g/cm^3}$	Muscle density (*39*)	$1.06\ \mathrm{g/cm^3}$
Poisson Ratio	0.5	k	$1 \times 10^8\ \mathrm{g/s^2}$
Kinetic Friction Coefficient	0.3	Static Friction Coefficient	0.42

Movie S1.

Muscle actuations of eBiobot with different frequencies. Real-time microscopic video showing the pillar deflections caused by muscle actuation in optical stimulations using 5 μ-ILEDs optogenetic device wirelessly at 10 W RF power, 50 ms pulse width and different operating frequencies (1, 2, 3, and 4 Hz). The left top caption indicates the applied frequencies. Scale bar: 2 mm.

Movie S2.

Modeling and simulation of eBiobot. Real time video showing the movement of the optimal eBiobot design obtained from the last iteration. The bot is stimulated at 4 Hz.

Movie S3.

Locomotion comparisons of eBiobot with different generations during design iteration. Videos showing walking locomotion of different generations of eBiobots, integrated with the μ-ILEDs optogenetic device, during wireless optical stimulation: 10 W RF power, 4 Hz 50 ms pulse width illumination pattern. 5 μ-ILEDs were used for the 2nd (top right), 3rd (bottom left), and 4th (bottom right) generations of eBiobots while a single μ-ILED was used for the 1st generation (top left). The movies are playing 2 times faster than real-time. Scale bars: 2 mm.

Movie S4.

Wireless μ-ILEDs driven walking of eBiobot. Real time video of walking eBiobot, integrated with 5 μ-ILEDs optogenetic device, during wireless optical stimulations: 10 W RF power, 4 Hz 50 ms pulse width illumination pattern. Scale bar: 2 mm.

Movie S5.

Walking of eBiobot with different frequencies. Real time videos of walking eBiobot, integrated with 5 μ-ILEDs optogenetic device, during wireless optical stimulation with different frequencies (1 Hz for top left, 2 Hz for top right, 3 Hz for bottom left, and 4 Hz for bottom right), 50 ms pulse width and 10 W RF power. The captions indicate applied frequencies. Scale bars: 2 mm.

Movie S6.

Walking of eBiobots depending on the number of μ-ILEDs. Real time videos of three groups of walking eBiobots: stimulated by a single μ-ILED (Sample A, B, and C from the left in top panel) and 5 μ-ILEDs (Sample A, B, and C from the left in bottom panel). All samples were stimulated with 4 Hz 50 ms pulse width and 10 W RF power. Scale bars: 2 mm.

Movie S7.

Walking of eBiobot depending on the rotation angle of the 5 μ-ILEDs spatial distribution. Real time videos of walking eBiobot integrated with 5 μ-ILEDs optogenetic device with different rotation angle:10 W RF power and 4 Hz, 50 ms pulse width. The top left and right captions of each panel indicate the rotation angle for 5 μ-ILED spatial distribution with respect to the central muscle actuator. Scale bars: 2 mm.

Movie S8.

Plow attached functional eBiobot like a snowplow. Walking video of the plow attached eBiobot, integrated with a 5 μ-ILEDs optogenetic device to remove out obstacles on the path. Wireless

optical stimulation: 4 Hz, 50 ms pulse width, and 10 W RF power. The movie is playing 8 times faster than real-time. Scale bar: 5 mm.

Movie S9.

Moving an object using functional eBiobot like a courier. Walking video of the collector attached eBiobot, integrated with a 5 μ-ILEDs optogenetic device to transport an object. Wireless optical stimulation: 4 Hz, 50 ms pulse width, and 10 W RF power. The movie is playing 4 times faster than real-time. Scale bar: 5 mm.

Movie S10.

Modeling and simulation of bipedal eBiobot. Real time video showing the turning motion of the bipedal eBiobot under differential stimulation. Left and right legs are being stimulated at 4 Hz and 1 Hz, respectively.

Movie S11.

Turning capabilities of bipedal eBiobots. Left-top and bottom panels show bipedal eBiobots stimulated with asynchronous mode to produce counterclockwise turning: 1 Hz 50 ms pulse width and 4 Hz 50 ms pulse width for left and right legs, respectively. Middle-top and bottom panels show bipedal eBiobot stimulated with synchronous mode to produce straight locomotion: 4 Hz 50 ms pulse width and 4 Hz 50 ms pulse width in both legs. Right-top and bottom panels show bipedal eBiobot stimulated with asynchronous mode to produce clockwise turning: 4 Hz 50 ms pulse width and 1 Hz 50 ms pulse width for left and right legs, respectively. Left-top captions in the video panels indicate the stimulation scheme and sample name. The movie is playing 4 times faster than real-time. Scale bars: 1 cm.

Movie S12.

Straight walking and turning of bipedal eBiobot. Real-time videos of walking bipedal eBiobot stimulating at 1 Hz and 4 Hz from 0 to 6 seconds, 4 Hz and 4 Hz from 7 to 13 seconds and 1 Hz and 4 Hz from 14 to 27 seconds for left and right legs respectively: 50 ms pulse width used in all cases. Its walking speed from 7 to 13 seconds was 1.75 mm/sec, setting the speed record again among bio-hybrid walkers with the largest body size among all bio-hybrid robots (table S1). Scale bar: 1 cm.

Movie S13.

Turning bipedal eBiobot that go through barriers course – Case I. Walking video of bipedal eBiobot that goes through obstacles course when stimulated at 4 Hz and 1 Hz for left and right legs respectively: 50 ms pulse width used in all cases. The movie is playing 10 times faster than real-time. Scale bar: 1 cm.

Movie S14.

Turning bipedal eBiobot that go through barriers course – Case II. Walking video of bipedal eBiobot that goes through obstacles course stimulated at 1 Hz and 4 Hz for initial 80 seconds, followed by switching of stimulation at 4 Hz and 1 Hz from 80 to 120 seconds for left and right legs respectively. After 120 seconds, a set of 4 Hz and 2 Hz of stimulations for left and right legs, respectively, was applied: 50 ms pulse width used in all cases. The movie is playing 10 times faster than real-time. Scale bar: 1 cm.

Movie S15.

Operations modes of dual panels of μ-ILEDs with gaming controllers. Real time video showing independent control of the light stimulation patterns of 3 bipedal μ-ILEDs devices and operations with 3 gaming controllers paired to each device.

Movie S16.

Swarming of multiple eBiobots using console system. Walking video of 3 bipedal eBiobots remotely controlled by 3 corresponding gaming controllers and console setup. The movie is playing 2 times faster than real-time. Scale bar: 1 cm.